Journal of Energy Storage 126 (2025) 117046

Contents lists available at ScienceDirect

Journal of Energy Storage

journal homepage: www.elsevier.com/locate/est

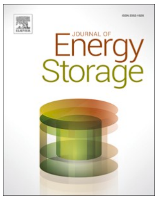

Research papers

Enhanced electrochemical performance of renewable flexible supercapacitors through the synergistic effects of nitrogen-doped carbonaceous fillers and controlled polypyrrole nanostructuring on nanocellulose fibers

Tomáš Lapka [a], Petr Mazúr [a], Jan Prokeš [b], Miloslav Lhotka [c], Marek Jurča [d], Marcela Dendisová [a], Ondřej Jankovský [e], Fatima Hassouna [a,*]

[a] *Faculty of Chemical Engineering, University of Chemistry and Technology, Prague, 166 28 Prague 6, Czech Republic*
[b] *Faculty of Mathematics and Physics, Charles University, 180 00 Prague 8, Czech Republic*
[c] *Faculty of Chemical Technology, University of Chemistry and Technology, Prague, 166 28 Prague 6, Czech Republic*
[d] *Centre of Polymer Systems, Tomas Bata University in Zlín, 760 01 Zlín, Czech Republic*
[e] *Department of Inorganic Chemistry, Faculty of Chemical Technology, University of Chemistry and Technology, 166 28 Prague 6, Czech Republic*

ARTICLE INFO

Keywords:
Cellulose nanofibers
Polypyrrole nanotubes
Nitrogen-doped 1-D carbonaceous fillers
Cellulose hydrogel separator/electrolyte
Renewable supercapacitor
Electrochemical performance

ABSTRACT

The growing demand for sustainable, high-performance energy storage solutions has driven advancements in flexible supercapacitors, which offer high power density, fast charging, and adaptability. This study investigates the electrochemical performance of novel, renewable, flexible, lightweight, and cost-effective electrodes synthesized using environmentally friendly one-pot and two-step methods. The electrodes integrate polypyrrole nanotubes (PPy–NT), cellulose nanofibers (CNF), and nitrogen-doped one-dimensional carbonaceous fillers (ACT–NT) or commercial carbon black. ACT–NT obtained by carbonizing and activating of PPy–NT, exhibit a nanotubular structure, high surface area, wettability, and tunable electrical conductivity. To construct a flexible supercapacitor, a simple cellulose hydrogel was synthesized as a dual-function electrolyte reservoir and separator. The PPy–NT/CNF electrode, synthesized via the one-pot method, achieved the highest initial specific capacitance (e.g., 172 F g^{-1} at 5 mV s^{-1}). This performance was attributed to the uniform growth of PPy–NT on CNF, which improved conductivity and redox activity. However, electrodes with carbonaceous fillers demonstrated better cycling stability by reinforcing the electrode structure and enabling a combination of electric double-layer capacitance and pseudocapacitive charge storage. The two-step synthesis method further enhanced the performance of PPy–NT/ACT–NT/CNF electrode by achieving an optimal balance of conductivity, morphology, wettability, textural and mechanical properties, outperforming their one-pot synthesis counterparts. These findings highlight the importance of material design for flexible, renewable supercapacitors, offering a pathway to more sustainable and efficient energy storage.

1. Introduction

Recent years have seen growing emphasis on environmental ecosystems and the need for sustainable energy development. The current imperative revolves around the design and advancement of energy storage devices with a dual emphasis on environmental friendliness and high performance. This involves the use of renewable materials and the continuous effort to improve energy efficiency [1]. Flexible supercapacitors have gained considerable attention due to their high power density, fast charging capabilities, and ability to withstand significant mechanical deformation, such as bending and twisting. These attributes make them well-suited to meet the requirements of modern portable and wearable electronics [2,3]. Electrodes of flexible supercapacitors are manufactured by integrating an electrochemically active material into a flexible matrix [4]. The use of renewable resources, such as cellulose-derived materials, as a flexible matrix for developing supercapacitor electrodes has emerged as an appealing alternative to fossil fuel-based materials [5,6]. Cellulose nanofibers (CNF), derived from natural

---

* Corresponding author.
E-mail address: fatima.hassouna@vscht.cz (F. Hassouna).

https://doi.org/10.1016/j.est.2025.117046
Received 6 February 2025; Received in revised form 14 April 2025; Accepted 10 May 2025

cellulose, have attracted significant interest due to their favourable characteristics. These include a high aspect ratio, remarkable mechanical properties (e.g., intrinsic flexibility and a Young's modulus of up to 250 GPa), low density, and a smooth and reactive surface [7,8]. CNF serve a dual function by acting as a robust mechanical framework that can withstand high deformation and as a reservoir for liquid electrolyte, facilitating ion transport. This dual role enhances the specific capacitance of the electrode, thereby improving the overall performance of the supercapacitor. [7,9–12]. Various electrochemically active substances, such as electrically conducting polymers, carbonaceous materials, and metal oxides, are often combined with CNF to prepare flexible electrodes for supercapacitors [4,13–16]. Among electrically conducting polymers, polypyrrole (PPy) is recognized as a promising material for developing pseudocapacitive electrode materials in supercapacitors. This is due to its easily achievable low-cost synthesis, non-toxicity, environmental stability, tuneable morphology (one-, two-, and three-dimensional), controllable electrical conductivity (ranging from 10^{-10} up to 10^4 S cm^{-1} with various dopants and levels of doping), interesting redox properties, and a high theoretical specific capacitance ($\sim$620 F g^{-1}) [17–20]. Moreover, its facile integration into a CNF matrix allows for the design of flexible, lightweight, and free-standing electrodes, as the two components can form interfacial interactions through hydrogen bonding [18,21]. Nevertheless, the primary obstacle to the practical application of PPy-based electrodes lies in their inadequate cycling stability, attributed to volumetric swelling and shrinking during the charge/discharge process [22,23]. This volumetric change compromises the integrity of the PPy backbone, leading to structural damage of the electrode and, consequently, a rapid capacitance decay [24,25]. Recently, nanostructured PPy, combined with carbonaceous fillers such as activated carbon, graphene, and carbon nanotubes, has emerged as a viable strategy to tackle these challenges [26–28]. The synergistic interaction between carbonaceous fillers and PPy nanostructures introduces an electric double layer capacitance (EDLC) charge storage mechanism to the electrode, complementing the pseudocapacitive behavior of PPy [29]. For instance, studies have shown that growing PPy nanostructures on the surface of carbonaceous materials (e.g., graphene, activated carbon, porous carbon, and carbon nanotubes) results in enhanced capacitance and cycling stability compared to neat PPy [30–32]. While this approach shows significant potential for enhancing supercapacitor performance, challenges associated with the hydrophobic nature of the carbonaceous fillers still persist. These challenges include the limited chemical compatibility of carbonaceous fillers with CNF, their poor dispersion in aqueous solutions during electrode preparation, which leads to the formation of heterogeneous filler network, and their lack of wettability by aqueous electrolytes during electrochemical processes. These factors negatively affect electron transfer pathways and ultimately compromise the overall electrochemical performance. The incorporation of heteroatoms (e.g., oxygen and nitrogen) into the carbon lattice of the carbonaceous fillers is expected to resolve both the dispersion and the wettability issues, consequently improving the electrochemical performance [33–35]. The most favourable heteroatom is nitrogen, which has a similar atomic size to carbon [36,37]. When doped into carbonaceous fillers, nitrogen introduces donor states near the Fermi level [38]. Furthermore, nitrogen boosts the reactivity of the carbonaceous fillers, promoting enhanced interaction of the carbon surface with PPy and CNF [39,40]. Insertion of heteroatom like nitrogen into carbonaceous fillers often necessitates time-consuming and laborious surface chemical treatment [41]. Furthermore, this chemical treatment can have a detrimental impact on their electrical conductivity [42,43]. Herein we propose and explore a straightforward strategy for the development of novel, flexible, and lightweight electrodes, involving nanostructures of PPy, CNF and distinctive nitrogen-doped one-dimensional nano-carbonaceous fillers, following a one-pot or two-step synthesis. The one-pot method involves the in situ polymerization of nanotubular PPy nanostructures (designed as PPy–NT) in the presence of structure guiding agent, CNF, and nitrogen-doped one-dimensional nano-carbonaceous fillers, all within an environmentally friendly medium. This novel process enables the simultaneous self-nanostructuring of PPy with tailored morphology (i.e., PPy–NT) and co-deposition on the surface of both CNF and nitrogen-doped one-dimensional nano-carbonaceous fillers, thus ensuring the formation of continuous conductive pathway within the electrode. In the two-step method, the process starts with the in situ polymerization of PPy–NT in the presence of structure guiding agent and CNF, followed by the addition of the nitrogen-doped one-dimensional nano-carbonaceous fillers. The nitrogen-doped one-dimensional nano-carbonaceous fillers were synthetized through the carbonization and chemical activation of pre-synthesized nanostructures of PPy–NT (designed as ACT–NT). ACT–NT encompass a range of advantageous features, including ease of synthesis, dispersion in an aqueous medium, improved wettability, large specific surface area, low density, and chemical compatibility with CNF. This compatibility is achieved through the establishment of electrostatic interactions between the nitrogen functional groups from ACT–NT and the hydroxyl/carboxyl groups from CNF. Unlike commercial carbon nanotubes (CNT), which are inherently hydrophobic and require extensive surface treatments for dispersion in water, ACT–NT naturally incorporate nitrogen groups into their carbon lattice, which eliminates the need for such modifications. These treatments, often labor-intensive and time-consuming [41], can also degrade the electrical conductivity of CNT [42,43]. Electrodes free of carbonaceous fillers, as well as those incorporating commercial carbon black (CB), were synthesized to provide further insights into the charge storage mechanisms of PPy–NT-based systems. To the best of our knowledge, no prior study has explored or compared these two methods. This work investigates the influence of synthesis methodology and nitrogen doping on the electrochemical performance of the electrodes and flexible supercapacitors.

In order to construct a fully renewable and flexible supercapacitor, we also developed cellulose hydrogel electrolyte, using a simple, and highly reproducible methodology. Hydrogel electrolytes have been lately emerged [44–46] and recognized with favourable application in the next generation of flexible supercapacitors [47]. Among the commonly used gel polymer electrolytes, poly(vinyl alcohol)-based hydrogel electrolytes have been widely utilized with both acidic and alkaline aqueous solutions [48]. However, most existing hydrogel electrolytes are petroleum-based, leading to a growing demand for those derived from renewable resources. Given the attractive features of cellulose, the development of cellulose hydrogel electrolytes that offer stretchability, flexibility, stable cycling, and non-leakage properties holds great potential for applications in the next generation of flexible supercapacitors [49,50]. In this study, we assembled renewable supercapacitor using PPy–NT-based electrodes and a cellulose hydrogel electrolyte, which also served as an electrochemical separator.

2. Experimental part

2.1. Materials

Cellulose nanofibers (CNF, 3 wt%) were kindly provided by Weidmann Fiber Technology (Switzerland). Pyrrole (98 %), 4-[4-(dimethylamino)phenylazo]benzenesulfonic acid sodium salt (methyl orange, M_w = 327.33), cellulose fibrous (medium), and Iron(III) chloride hexahydrate ($\geq$ 99 %) were purchased from Merck (Germany). Potassium hydroxide (KOH), sodium hydroxide (NaOH), and urea pellets were bought from PENTA (Czech republic) 35 wt% hydrochloric acid (HCl) and 96 wt % sulfuric acid (H_2SO_4) were purchased from Lach-Ner (Czech republic). Carbon black (CB, Black Pearls 2000) was kindly donated by Cabot (USA). All chemicals were used as received. Deionized water was used in the experiments.

2.2. *Materials preparation*

2.2.1. *Synthesis of activated polypyrrole nanotubes*

PPy–NT precursor was prepared following the procedure outlined in [51] (see details in the supplementary material).

The activation of PPy–NT (ACT–NT) involved a two-step process, beginning with high-temperature carbonization followed by KOH treatment. Initially, PPy–NT underwent carbonization in a horizontal tube furnace (Carbolite Gero) under a nitrogen atmosphere at a heat rate of 10 °C min^{-1} at two different temperatures, i. e., 850 °C and 1000 °C. Upon reaching the desired temperature, the sample was cooled under nitrogen flow. The carbonized PPy–NT (CPPy–NT) were designated as CPPy–NT@850 and CPPy–NT@1000. Each carbonized sample was then immersed in a 7 M KOH solution and mixed for 12 h to facilitate the diffusion of KOH into the pore network. After thorough mixing, the solution was filtered without rinsing to maintain the KOH within the pores, and the samples were dried in an oven at 60 °C. The samples then underwent an additional carbonization cycle at 750 °C, with a heating rate of 10 °C min^{-1} in a nitrogen atmosphere, to complete the activation process. Finally, the samples were thoroughly washed with a 0.5 M HCl solution and deionized water. The resulting powders were labelled as ACT–NT@850 and ACT–NT@1000.

2.2.2. *Elaboration of PPy–NT-based electrodes*

Hybrid PPy–NT-based electrodes were prepared using our newly developed one-pot synthesis method [52] with slight modifications, as well as a two-step approach.

One-pot synthesis: This process involved the in situ chemical oxidative polymerization of pyrrole in the presence of methyl orange as a structure guiding agent, along with CNF and carbonaceous fillers (i.e., ACT–NT or CB). In a standard procedure, 11.3 g of 3 wt% CNF gel was dispersed with 50 ml of deionized water, stirred at 300 rpm, and cooled to 5 °C in an ice bath. Then, 0.13 g of the carbonaceous fillers, 65 mg of methyl orange, and 0.25 ml of pyrrole were added to the mixture, maintaining a 2:1 weight ratio of pyrrole to carbonaceous filler and a 1:1 weight ratio of the active material (i.e., PPy–NT/carbonaceous filler) to CNF (Table S1). These ratios were optimized based on preliminary screening to achieve the optimal balance of mechanical and electrochemical properties. The mixture was stirred for 30 min. The polymerization reaction was then initiated by the dropwise addition of 3.4 g of Iron (III) chloride hexahydrate dissolved in 50 ml of water. The Iron (III) chloride solution was pre-cooled to 5 °C before being added to the reaction mixture, which was stirred for 12 h. Afterward, the product was filtered and thoroughly washed with 0.1 M HCl, acetone, and deionized water until the filtrate became transparent. The resulting filtration cake was resuspended in 70 ml of deionized water and casted onto a PTFE Petri dish, then dried for several days to form a flexible electrode film. The electrodes were designated as PPy–NT/carbonaceous filler/CNF, e.g., PPy–NT/ACT–NT@850/CNF. Reference flexible electrode without carbonaceous fillers was also prepared following the same procedure. It was labelled as PPy–NT/CNF.

Two-step synthesis: The process began with the in situ chemical oxidative polymerization of pyrrole in the presence of methyl orange and CNF, followed by the addition of the ACT–NT@1000. Apart from this step, the fabrication procedure was identical to that used in the one-pot synthesis. Two electrodes were prepared with different weight ratios of the active material (i.e., PPy–NT/ACT–NT@1000 with a PPy–NT to ACT–NT@1000 ratio of 2:1) to CNF, namely, 1:1 and 2:3 (Table S1). These electrodes were labelled PPy–NT/ACT–NT@1000/CNF_TS1-1 and PPy–NT/ACT–NT@1000/CNF_TS2-3, respectively.

2.2.3. *Preparation of cellulose hydrogel*

Cellulose hydrogel was prepared via physical crosslinking method [47]. In brief, 1.5 g of NaOH and 2.5 g of urea were dissolved in 20 ml of deionized water. Then, 1.3 g of cellulose was added to NaOH/urea solution. The mixture was stirred at 800 rpm for 3 h and stored at −15 °C for 12 h. Afterward, the mixture was thawed and transferred into a thin PTFE mold, where it was kept at room temperature for two days to form a flexible cellulose hydrogel with the thickness of 2 mm. The hydrogel was subsequently washed via vacuum filtration with 0.5 M H_2SO_4 solution and stored in a 1 M H_2SO_4 solution to immobilize the electrolyte within the hydrogel. It is worth noting that the cellulose hydrogel also served as a separator during the assembly of the supercapacitor.

2.3. *Characterization methods*

A Dispersive Raman spectrometer, equipped with an InVia Reflex microscope, was employed to characterize the chemical structure of both the fillers (PPy–NT, CPPy–NT, ACT–NT and CB) and the PPy–NT-based electrodes before and after the galvanostatic charge discharge (GCD) cycles. The analysis was conducted using a laser power of 2 mW and an excitation wavelength of 785 nm. Each acquisition comprised 10 accumulations, each lasting 30 s. The final spectrum was generated from 10 acquisitions. The Fourier Transform Infrared (FTIR) spectra were measured using FTIR spectrometer iS50 (Nicolet, Thermo Fisher Scientific) equipped with an ATR (Attenuated Total Reflection) diamond crystal. The spectra were collected in mid IR region from 3000 to 400 cm^{-1}. 128 scans with 4 cm^{-1} resolution were recorded for one spectrum and at least 2 spectra were collected from each sample. X-Ray photoelectron spectroscopy (XPS) was employed to analyze the surface chemistry of the synthesized carbonaceous fillers. The analysis was performed using an Omicron Nanotechnology XPS device, equipped with a monochromatic Al lamp emitting radiation with an excitation energy of 1486.7 eV. The XPS spectra were deconvoluted using CasaXPS software. Scanning electron microscopy (SEM) analysis was performed using a Tescan Mira 3 LMH instrument, operating at 3 kV in secondary electron mode. This technique was employed to examine the microstructure of the cellulose hydrogel, and PPy–NT-based electrodes at their cross-sections. Transmission electron microscopy (TEM) imaging was performed using a model JOEL JEM-1010 instrument, operating at 100 kV. This technique was used to examine the morphology of the nanofillers (i.e., PPy–NT, CPPy–NT, ACT–NT and CB) at the nanoscale on a 300 copper grid. The textural properties of the nanofillers, including the specific surface area (S_{BET}), total pore volume, and pore size distribution, were determined using the nitrogen physisorption technique with a 3Flex analyser (Micromeritics, Norcross). Prior to nitrogen adsorption, the samples were degassed at 373 K to ensure a clean surface. The Brunauer-Emmett-Teller (BET) method was used to fit the adsorption isotherm. Total pore volumes were evaluated at a relative pressure of 0.95, while pore size distribution was determined using a density functional theory (DFT) model with nitrogen @ 77 on Carbon Slit Pores, as per the NLDFT approach. The Rouquerol criterion was applied to enhance the validity of the calculations, ensure the linearity of the BET plot, and obtain a positive value for the constant C, which is used to calculate the monolayer capacity of the BET isotherm. A four-point Van der Pauw method was used to measure the room temperature electrical conductivity of the nanofillers and the PPy–NT-based electrodes. The equipment used included a Keithley 6221 DC and AC Current Source, a Keithley 2001 Multimeter, and a Keithley 7001 Switch System equipped with a Keithley 7011-S-Quad 1 • 10 multiplexer. The PPy–NT-based electrodes were tested as prepared. For powder samples, electrical conductivity was determined using the Van der Pauw method during compression in a cylindrical glass cell with an inner diameter of 1 cm. The sample was positioned between a glass piston carrying four platinum/rhodium electrodes around its circumference and an insulating ceramic base [53]. Tensile testing measurements were conducted using a Testometric universal-testing machine (M 350-5CT, Testometric Co. Ltd.) equipped with a 100 N load cell. The tensile properties of the films were examined with a crosshead speed of 0.5 mm min^{-1}, with a gauge length set at 50 mm. Three samples were extracted from each group for measurement (except for PPy–NT/ACT–NT@1000/CNF_TS2-3), and the reported value represents the average of these calculations. Young's modulus of tensile elasticity (*E*-modulus) was determined by analysing the linear part of the tensile curve within the range of 0.05–0.25 %, following standard procedures.

The electrochemical properties of the PPy–NT-based electrodes were evaluated using a Biologic VSP-300 potentiostat in a three-electrode and two-electrode configuration. For three-electrode configuration, a mercurous sulphate reference electrode (MSE) with a saturated K_2SO_4 inner electrolyte (0.65 V vs. SHE) and a platinum sheet counter electrode were employed. All the potentials within this work are referred vs. MSE. A 1 M H_2SO_4 solution was chosen as the suitable electrolyte. The electrodes were shaped into circles with a diameter of 6.4 mm. Cyclic voltammetry (CV) and GCD measurements were conducted. CV measurements were conducted within a potential range of −0.5 V to 0.15 V using various scan rates (200, 100, 20, 10, 5 mV s^{-1}). The capacitance was calculated from the cathodic part of the curve in the potential range of −0.2 V to 0.1 V by integrating the electric charge, as described in Eq. (1),

$$C = \frac{1}{Ev}\int_{E_1}^{E_2} i\,dE = \frac{1}{(E_2 - E_1)v}\int_{E_1}^{E_2} i\,dE \tag{1}$$

where *E* represents the electric potential window, with E_1, E_2 as its boundaries; *v* denotes potential scan rate, *i* represents the electric current; and *dE* is the potential difference. The calculated capacitance was divided by the total mass of the electrode in order to obtain specific capacitance. GCD measurements were conducted at various constant current densities (31.1, 15.5, 6.2, 3.1, 1.6 and 0.6 mA cm^{-2}) within a potential window of −0.5 V to 0.15 V to determine the specific capacitance under current load. GCD measurements were also performed at a constant current density of 6.2 mA cm^{-2} within the same potential windows for 500 cycles to assess the mid-term cycling stability of fresh PPy–NT-based electrodes. For selected electrodes, 500 GCD cycles mid-term stability test was also conducted at extended potential window of –0.5 V to 0.3 V in order to check the impact of nitrogen-doped carbonaceous fillers on electrochemical stability. The capacitance was calculated from Eq. (2),

$$C = \frac{Q_{max}}{(E_2 - E_1)} \tag{2}$$

where Q_{max} represents the maximal electric charge achieved on the discharge curve. The specific capacitance was recalculated in the same method as for the CV measurements.

The electrochemical performance of the PPy–NT-based electrodes was also evaluated in a symmetric two-electrode configuration using a custom-designed T-cell. The supercapacitor device was assembled using a round shaped cellulose hydrogel electrolyte, which also served as a separator, and two round-shaped electrodes of the same material, each with a diameter of 0.8 cm (0.5 cm^2 of active area). The electrodes were soaked in a 1 M H_2SO_4. Following this, the electrodes and cellulose hydrogel electrolyte/separator were assembled into a standard supercapacitor geometry, with the cellulose hydrogel positioned between the two electrodes and compressed using graphite current collector sticks. The MSE reference electrode was also inserted to the T-cell via Luggin capillary to monitor the potential on both electrodes during the experiments. For comparison, the commercial membrane Cellgard 5550 was also tested with PPy–NT-based electrodes to evaluate the electrochemical performance relative to the cellulose hydrogel. The device underwent GCD cycling in a voltage range of 0 to 0.5 V at the same current densities used in the three-electrode configuration, i.e., 31.1, 15.5, 6.2, and 3.1 mA cm^{-2}. Before and after cycling, electrochemical impedance spectroscopy (EIS) was performed at open-circuit voltage over a frequency range of 100 kHz - 100 mHz with a voltage amplitude of 10 mV to assess the ohmic resistance of the supercapacitor. Mid-term stability testing of 500 GCD cycles was performed on selected samples at 6.2 mA cm^{-2}.

The specific capacitance from the two-electrode configuration was calculated using Eq. (3),

$$C_{sp} = \frac{Q_{discharge}}{(U_{max} - U_{min}) \bullet m} \tag{3}$$

where U_{min} and U_{max} are the minimum and maximum voltage limits used in the GCD measurement, and *m* is the total mass of both electrodes.

The Coulombic efficiency (*CE*), energy efficiency (*EE*) and voltage efficiency (*VE*) of a GCD cycle were calculated according to Eqs. (4), (5) and (6),

$$CE = \frac{Q_{charge}}{Q_{discharge}} \tag{4}$$

$$EE = \frac{E_{charge}}{E_{discharge}} \tag{5}$$

$$VE = \frac{EE}{CE} \tag{6}$$

where Q_{charge} and $Q_{discharge}$ are the electrical charges charged and discharged during the cycle, and E_{charge} and $E_{discharge}$ are the energies associated with the charging and discharging phases of the cycle, respectively. The evaluation of integral charges and energies for individual half-cycles was carried out using the analytical tool of EC-lab software (Biologic). The efficiency values were averaged from all recorded cycles within a given series. The capacity decay was calculated from the slope of the linear part of $Q_{discharge.}$ vs. cycle number dependency.

The energy density of PPy–NT supercapacitors was calculated according to Eq. (7),

$$E = \frac{1}{2}C_{sp} \bullet U \tag{7}$$

where C_{sp} is calculated specific capacitance according to Eq. (3) and *U* is applied voltage window.

Power density was evaluated according to Eq. (8),

$$P = \frac{E}{\Delta t} \tag{8}$$

where *E* is energy density calculated according to Eq. (7) and Δt is discharge time.

Equivalent series resistance (ESR) from GCD cycles was calculated according to Eq. (9)

$$ESR = \frac{\Delta U}{2I} \tag{9}$$

where ΔU is voltage drop at the charge/discharge switch and I is applied constant current.

3. Results and discussion

The proposed strategy for developing a fully renewable supercapacitor, using flexible PPy–NT-based electrodes and cellulose hydrogel electrolyte, which also functions as the device separator, is illustrated in Fig. 1.

3.1. Chemical structure and morphology of the cellulose hydrogel

A variety of solvent systems can be utilized to dissolve cellulose, including ionic liquids and alkali/urea systems, e.g., sodium hydroxide/urea (NaOH/urea) solution [54,55]. The NaOH/urea aqueous solution is notable for its environmental sustainability, simplicity, low toxicity, and cost-effectiveness. NaOH, being a strong base, disrupts hydrogen bonds between cellulose chains, while urea, a potent hydrogen bond disruptor, further aids in breaking both intra- and intermolecular hydrogen bonds in cellulose [54,55]. Cellulose hydrogel was prepared via physical

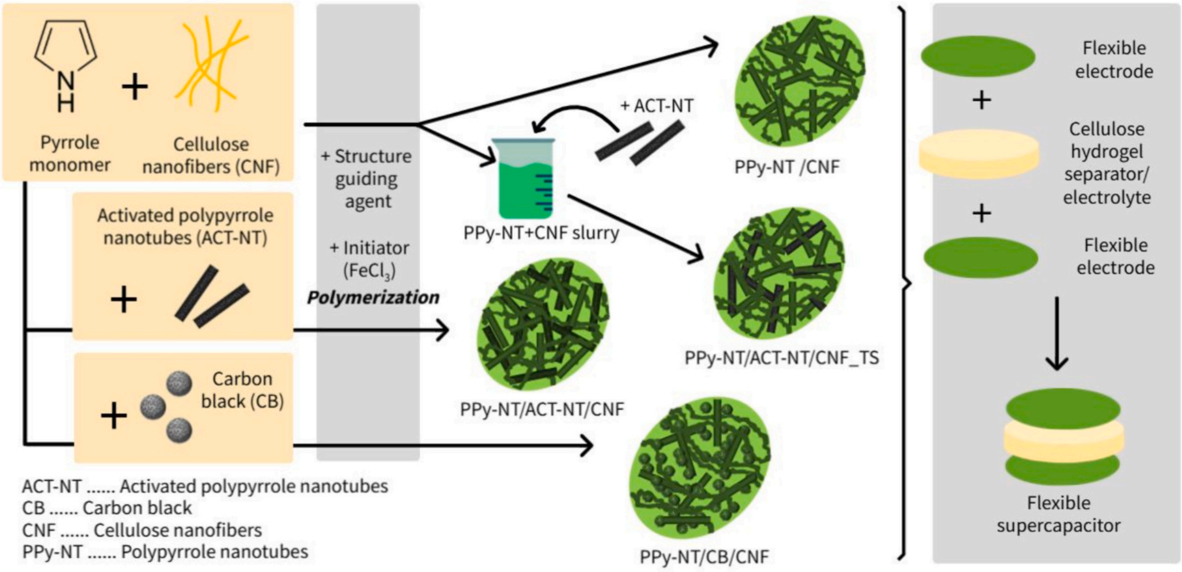

Fig. 1. Schematic representation of flexible PPy–NT-based electrode preparation and supercapacitor assembly.

crosslinking method using the freeze-thaw method. Fig. 2a illustrates the interactions that occur during the crosslinking process between the cellulosic chains and the NaOH/urea. Photographs of the prepared cellulose hydrogel soaked in 1 M H_2SO_4 are shown in Fig. 2b. The FTIR spectra of pure cellulose and freeze dried cellulose hydrogel are depicted in Fig. 2c. These spectra highlight the differences between the chemical structures of both forms of cellulose as a result of the gelation process. FTIR spectrum of the cellulose hydrogel shows the typical cellulose bands, along shifts that occur after NaOH treatment [56]. The full assignments of pure cellulose and cellulose hydrogel spectra can be found in Table S2. The SEM image of the cellulose hydrogel, shown in Fig. 2d, reveals its porous structure, which facilitates ionic permeability and

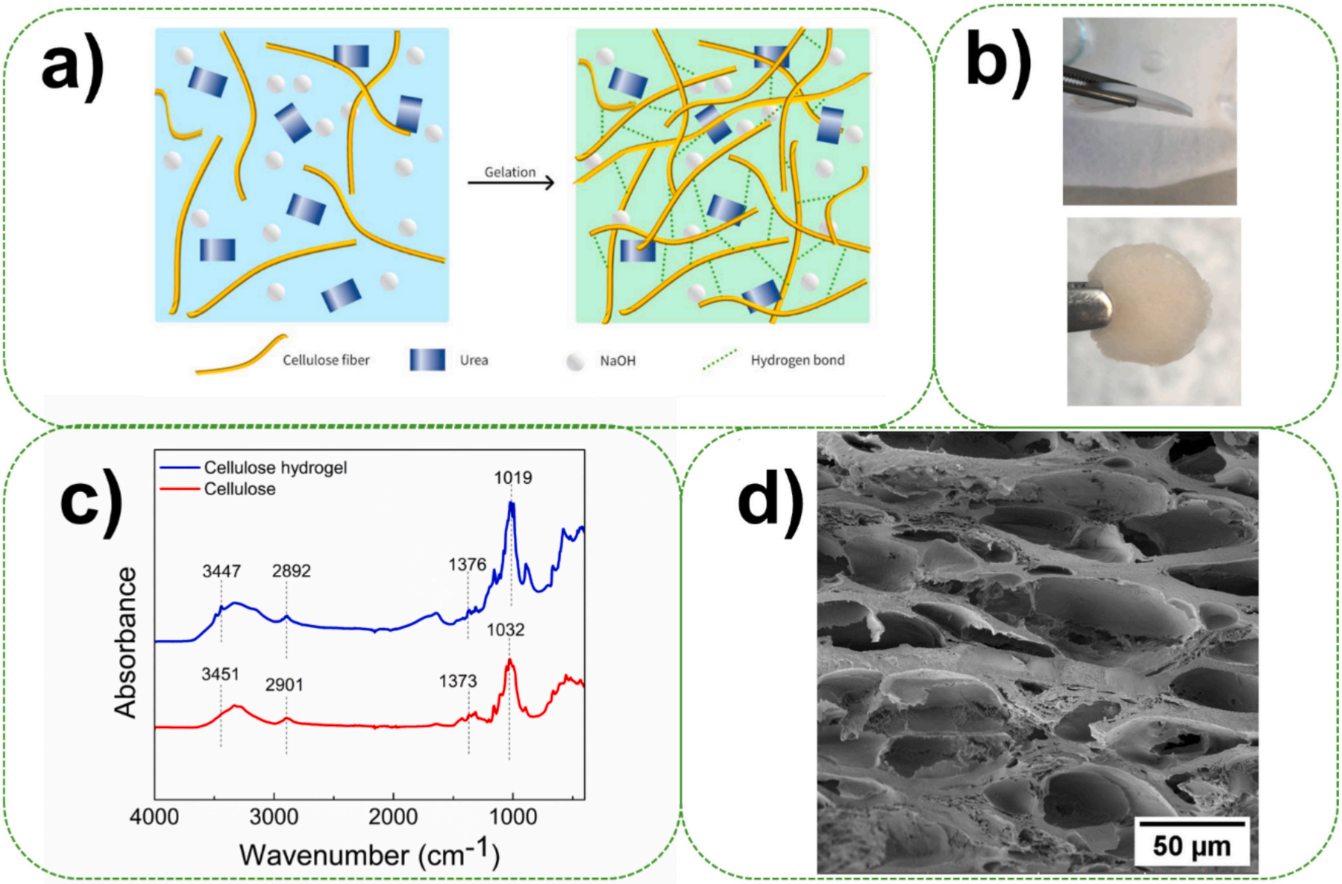

Fig. 2. a) Schematic representation of cellulose hydrogel preparation and the mechanism of gelation, b) Photographs of cellulose hydrogel, c) FTIR spectra of pure cellulose and cellulose hydrogel, and d) SEM image of cellulose hydrogel.

transport, both constituting key attributes for enhancing electrochemical performance in supercapacitor applications.

3.2. Chemical and physical properties of the as-synthesized activated polypyrrole nanotubes

In our previous study [57] we investigated the effect of carbonization temperature (ranging from 650 to 1000 °C) during the carbonization of PPy–NT on the chemical and physical properties of the resulting carbonized PPy–NT (CPPy–NT). It was found that CPPy–NT@850 and CPPy–NT@1000 exhibited distinct differences in structure and properties. In this study, we aim to investigate how the KOH activation and carbonization process influence these characteristics, with a particular focus on textural properties such as specific surface area, nitrogen and graphitic N content, and electrical conductivity, all of which are essential for enhancing the specific capacitance of carbonaceous fillers.

The chemical structure and physical properties of PPy–NT and its carbonized derivatives, i.e., CPPy–NT and ACT–NT, as well as commercial CB were systematically examined. TEM images of ACT–NT@850, ACT–NT@1000 and their precursors (CPPy–NT@850 and CPPy–NT@1000) along with CB, are depicted in Fig. 3. The pristine PPy–NT (Fig. 3a) displayed a well-defined nanotubular morphology with an average diameter of approximately 60 nm. This structure is attributed to the templating effect of methyl orange/iron(III) complexes, which guide the anisotropic growth of PPy during in situ polymerization [58–61]. Remarkably, the tubular morphology was largely preserved during both carbonization and the activation processes used to produce ACT–NT (Fig. 3 b-e), indicating the structural robustness of the PPy–NT framework under high-temperature treatment and chemical activation. The commercial CB (Fig. 3f) exhibited a highly uniform distribution of spherical nanoparticles with an average diameter of about 20 nm, characteristic of its monodisperse morphology.

To monitor the changes in pore size distribution (PSD) and S_{BET} of PPy–NT before and after activation, the textural properties of the nanofillers were assessed using N_2 sorption analysis. Surface areas were determined using the BET equation, while pore size distributions were derived from the N_2 adsorption isotherm using DFT calculations. Fig. S1a and S1b illustrate the N_2 sorption isotherms, and PSD curves, respectively. Table 1 provides a summary of the textural properties. As shown in the N_2 sorption isotherms (Fig. S1a, Table 1), both PPy–NT and CPPy–NT exhibited a typical type II isotherm according to the Bruner-Deming-Deming-Teller classification. They also displayed the lowest S_{BET} (45, 52 and 68 $m^2 \cdot g^{-1}$ with PPy–NT, CPPy–NT@850 and CPPy–NT@1000, respectively), very low mesoporosity close to zero and no microporosity. After KOH activation of CPPy–NT, a transition in the adsorption isotherms from type II to type IVa occurred, indicating the formation of high-surface-area hierarchically porous materials with both micro- and mesopores. As summarized in Table 1, ACT–NT@850 displayed a balanced ratio of micropores to mesopores, while ACT–NT@1000 showed a higher proportion of micropores. This trend is further corroborated by the PSD curves (Fig. S1b). The activation process also led to a significant increase in S_{BET}, i.e., from 52 $m^2\ g^{-1}$ for CPPy–NT@850 to 1062 $m^2\ g^{-1}$ for ACT–NT@850, and from 68 $m^2\ g^{-1}$ for CPPy–NT@1000 to 761 $m^2\ g^{-1}$ for ACT–NT@1000. The decrease in S_{BET} for ACT–NT@1000 compared to ACT–NT@850 can be attributed to the chemical structure and composition of their respective precursors,

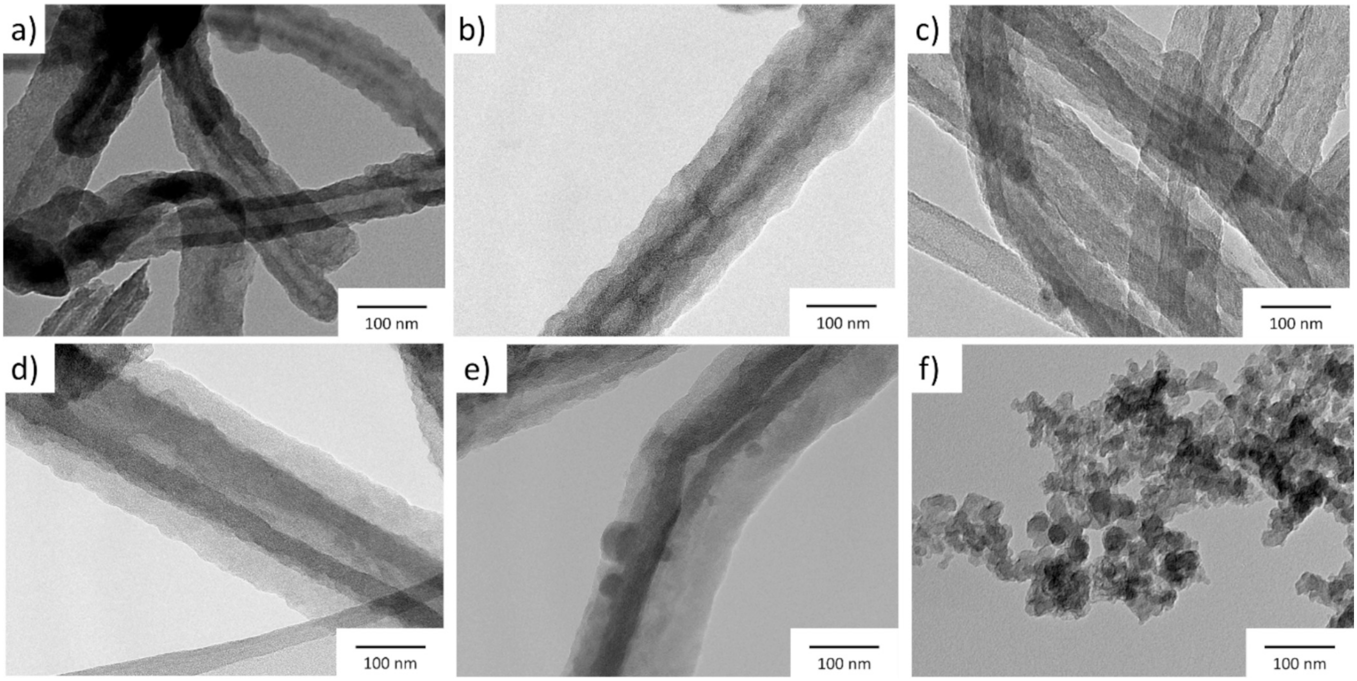

Fig. 3. TEM images of: a) PPy–NT, b) CPPy–NT@850, c) CPPy–NT@1000, d) ACT–NT@850, e) ACT–NT@1000, and f) CB.

Table 1
Textural properties of PPy–NT and the carbonaceous fillers.

Sample	S_{BET} ($m^2\ g^{-1}$)	$V_{total\ pore}$ ($cm^3\ g^{-1}$)	$V_{micropore}$ ($cm^3\ g^{-1}$)	$V_{mesopore}$ ($cm^3\ g^{-1}$)	Isotherm type
PPy–NT	45	0.08	0	0.08	II
CPPy–NT@850	52	0.09	0	0.09	II
CPPy–NT@1000	68	0.10	0.01	0.10	II
ACT–NT@850	1062	0.74	0.35	0.39	IVa
ACT–NT@1000	761	0.35	0.24	0.11	IVa
CB [4]	1416	1.78	0.28	1.5	Ib and IVa

CPPy–NT@850 and CPPy–NT@1000. CPPy–NT@1000 exhibits a higher degree of carbonization and reduced nitrogen content (see Table S5), which increases its hydrophobicity. This increased hydrophobicity hinders the diffusion of KOH aqueous medium into the pores of CPPy–NT@1000 during the activation process, resulting in lower surface area. It is worth noting that the commercial CB exhibited a type Ib and IVa with a higher S_{BET} of 1416 m^2 g^{-1} and a higher total pore volume, where mesopores predominated [4].

Fig. 4a depicts the Raman spectra of PPy–NT and the carbonaceous fillers (CPPy–NT, ACT–NT and CB). All carbonaceous fillers display characteristic peaks at 1598 cm^{-1} (G band), corresponding to sp^2-hybridized carbon, and 1314 cm^{-1} (D band), associated with structural defects [62]. The intensity ratio (I_D/I_G) calculated from the Raman spectra (Table S3) was 1.33 for CPPy–NT@850 and 1.43 for CPPy–NT@1000 [57]. The increase in the I_D/I_G ratio with higher carbonization temperature is attributed to the reduction of disorder in sp^2-hybridized carbon during the second stage of amorphization, leading to an increased content of graphitic domains [63]. Notably, the KOH activation did not significantly affect the I_D/I_G ratio. The Raman spectrum of PPy–NT shows characteristic peaks associated with its electrically conductive state. The full spectral assignments are provided in Table S4. XPS analysis (Table S5, Fig. 4b) revealed notable compositional differences between the PPy–NT precursor and its carbonized and activated counterparts. The XPS wide-survey spectra (Fig. S2) of pristine PPy–NT displayed five peaks at binding energies of 284.9, 532.4, 399.6, 198.0 and 168.4 eV, corresponding to C(1 s), O(1 s), N(1 s), Cl(1 s), and S (1 s), respectively. Following carbonization and subsequent KOH activation, only three main peaks of C(1 s), O(1 s) and N(1 s) remained. This reduction indicates the thermal degradation of dopant anion and methyl orange residues during high-temperature treatment. The C1(s) content increased from 74 % in the PPy–NT to 85 % in ACT–NT@850. Interestingly, the N(1 s) content remained relatively stable at 11 % for CPPy–NT@850 and 10 % for ACT–NT@850, comparable to 12 % in pristine PPy–NT. Upon increasing the carbonization temperature to 1000 °C, C(1 s) content further rose to 95 % for CPPy–NT@1000 and 90 % for ACT–NT@1000. This increase was accompanied by a marked decrease in nitrogen content, with N(1 s) dropping to 3 % for CPPy–NT@1000 and 2 % for ACT–NT@1000. Deconvolution of N(1 s) core level spectra (Fig. 4b, Fig. S3) showed discrepancies between the PPy–NT precursor and the carbonaceous materials, as well as among the various fillers. The PPy–NT exhibited three characteristic peaks attributed to pyrrolic N (-NH-), polaron (-NH+) and bipolaron (-NH++) at 399.5, 400.7, and 402.1 eV, respectively. These findings are in good agreement with Raman spectroscopy results. In contrast, all CPPy–NT and ACT–NT displayed four nitrogen peaks: pyrrolic N at 399.5 eV, pyridinic N at 398.5 eV, graphitic N at 400.9 eV and oxidized N at 401.9 eV. Notably, the content of graphitic N increased with higher carbonization temperatures, while KOH activation process did not significantly alter the distribution or proportion of the nitrogen species.

Fig. 4c-d compare the electrical conductivity of the carbonaceous fillers under varying applied pressures. The electrical conductivity measurements showed a direct correlation with increasing pressure, confirming that electrical contact and particle compaction influence conductivity behavior. The initial carbonization process led to a decrease in electrical conductivity (as observed for CPPy–NT) due to the loss of polarons and bipolarons, key charge carriers in conductive PPy–NT, confirmed by both XPS (Table S4) and Raman spectroscopy (Fig. 4a). However, electrical conductivity improved markedly with increasing carbonization temperature. As previously reported [57], higher temperatures induce structural transformations in CPPy–NT, enhancing graphitization and, consequently electrical conductivity [64]. This trend was supported by XPS results (Fig. 4b) showing an increased fraction of graphitic N species In graphitic domains, p–π conjugation between nitrogen lone pairs and the π-electron system of carbon improves charge transport, thereby enhancing the overall conductivity of nitrogen-doped carbon materials [38,65].

For a given CPPy–NT, a decrease in electrical conductivity is observed after the KOH activation process. This reduction is due to KOH etching the nanotubes, which creates defects in the nanotube walls, disturbing the conductive pathways. Similar effects have been reported

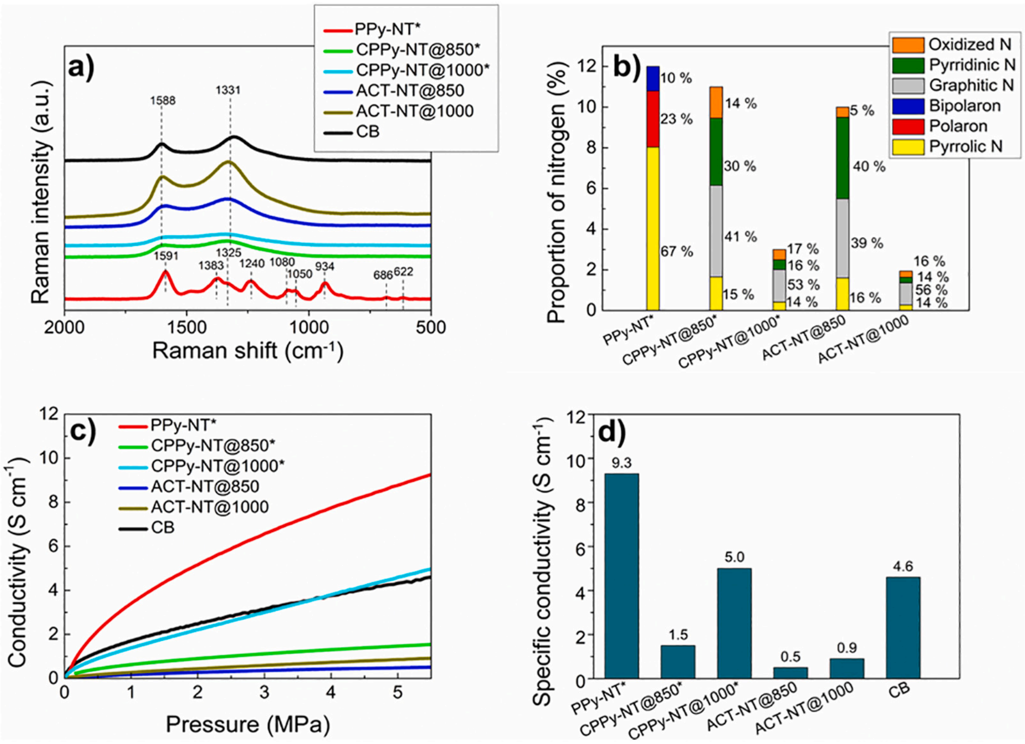

Fig. 4. Characterization of PPy–NT and carbonaceous fillers: a) Raman spectroscopy, b) XPS summary of N(1 s) core spectra, c) dependence of electrical conductivity on applied pressure, and d) electrical conductivity at a pressure of 5.5 MPa. *: [57].

in the literature for carbon nanotubes [66]. Notably, the electrical conductivity of CB is higher than that of all ACT–NT. Overall, ACT–NT@1000 exhibit a higher content of graphitic N and improved electrical conductivity compared to ACT–NT@850, but with a lower S_{BET}. In contrast, ACT–NT@1000 display both lower electrical conductivity and S_{BET} compared to CB.

3.3. Micro-structure of the PPy–NT-based electrodes and performance-related characteristics

Photographs of the prepared flexible PPy–NT-based electrode films, with an average thickness of 150 μm are depicted in Fig. S4. The presence of nitrogen moieties in the ACT–NT lattice enhances its dispersion in aqueous solution during composite preparation and electrode formation. As a result, ACT–NT was successfully incorporated into PPy–NT-based electrodes using both synthesis methods. Conversely, achieving good dispersion of CB in aqueous solution proved challenging due to its hydrophobic nature (Table S4). Moreover, the incorporation of CB during the two-step synthesis of PPy–NT-based electrodes proved unsuccessful, as CB gradually leached out of the electrode. This is likely attributed to its zero-dimensional nanoscale size (20 nm) and insufficient integration into the electrode matrix. The SEM images of CNF and PPy–based electrode films are shown in Fig. 5a-g. The pure CNF flexible film displays a compact structure composed of highly interconnected nanofibers (Fig. 5a). The SEM image of PPy–NT/CNF (Fig. 5b) reveals the formation of PPy with a nanotubular morphology on the surface of CNF during the in situ polymerization of pyrrole in the presence of methyl orange. This highlights the crucial role of methyl orange as a primary template, guiding the nanotubular structure, while CNF acts as the substrate and secondary template for PPy–NT. The addition of carbonaceous fillers during the in situ polymerization did not affect the nanotubular morphology of PPy–NT (Fig. 5c-e). Close inspection reveals better dispersion of the nanotubular ACT–NT, along with PPy–NT and CNF (Fig. 5d-e), compared to CB spherical particles (Fig. 5e), where large CB aggregates are visible. PPy–NT deposited on CNF and ACT–NT formed a more entangled and uniform network. The in situ generated PPy–NT is nearly indistinguishable from ACT–NT, suggesting that ACT–NT may have served as a secondary template during polymerization. In contrast, due to the zero-dimensional nanoscale size (20 nm) of CB and its compatibility with PPy–NT, PPy–NT/CB/CNF exhibits a more compact microstructure, with PPy–NT uniformly coating both CB and CNF surfaces. When ACT–NT are added after pyrrole polymerization in the presence of CNF, i.e., PPy–NT/ACT–NT@1000/CNF_TS1–1 and PPy–NT/ACT–NT@1000/CNF_TS2–3 (Fig. 5f-g), they exhibit high dispersion and form a well-entangled, interconnected network with PPy–NT deposited on CNF. This is due to the establishment of strong intermolecular interactions, such as π-π stacking and electrostatic interactions [13]. Overall, all prepared PPy–NT-based electrodes display a porous network, which is advantageous for electrolyte diffusion. Raman spectroscopy (Fig. S5) confirmed the chemical structure of the prepared electrodes. The Raman spectra, recorded at 785 nm excitation (resonance with the delocalized bipolarons and polarons) [51,67], consistently showed features corresponding to the oxidative form of PPy–NT, regardless of composition or synthesis method. A complete spectral assignment is provided in Table S2.

The effects of composition and preparation method on the mechanical properties of the PPy–NT-based electrode films were examined. The stress-strain curves, along with the extracted Young's modulus, ultimate tensile strength and elongation at break are depicted in Fig. S6a-S6d. The addition of carbonaceous fillers to PPy–NT/CNF via a one-pot synthesis reduced Young's modulus and increased ultimate tensile strength. The decrease in Young's modulus was more pronounced in PPy–NT/CB/CNF (from 256 ± 43 for PPy–NT/CNF to 115 ± 17 MPa), likely due to the stiffness [68] and poor dispersion of CB in the PPy–NT/CNF matrix, as observed in SEM images. In contrast, PPy–NT/ACT-NT/CNF exhibited higher ultimate tensile strength than PPy–NT/CB/CNF and PPy–NT/CNF, attributed to the superior strength [69] and better dispersion of ACT-NT within the composite. Despite having the same composition, PPy–NT/ACT–NT/CNF and PPy–NT/ACT–NT@1000/CNF_TS1–1 exhibited different mechanical properties, influenced by their synthesis method. The two-step synthesized PPy–NT/ACT–NT@1000/CNF_TS1–1 displayed the highest Young's modulus (329 ± 35 MPa) and ultimate tensile strength (7.5 ± 0.3 MPa) among all films, resulting in superior mechanical stiffness and strength,

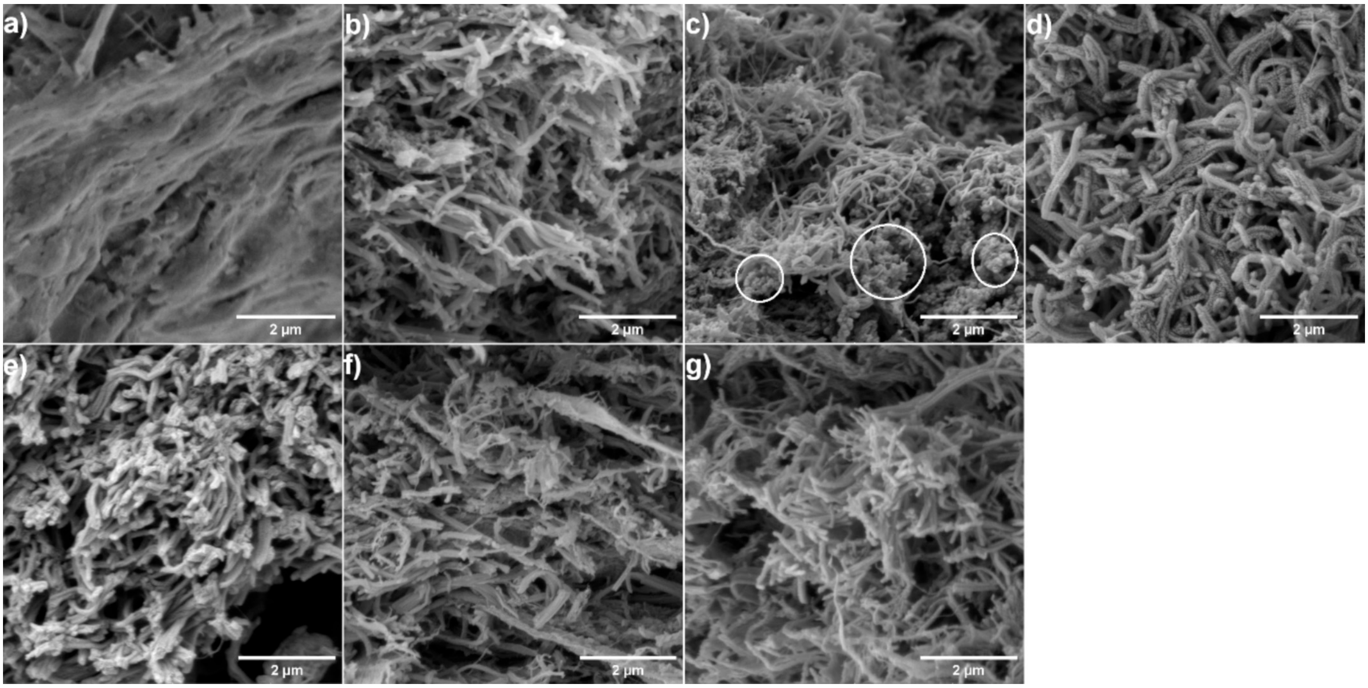

Fig. 5. SEM images of the electrode films: a) CNF, b) PPy–NT/CNF, c) PPy–NT/CB/CNF, d) PPy–NT/ACT–NT@850/CNF, e) PPy–NT/ACT–NT@1000/CNF, f) PPy–NT/ACT–NT@1000/CNF_TS1-1, and g) PPy–NT/ACT–NT@1000/CNF_TS2-3.

comparable to pure CNF film [52]. In PPy–NT/ACT–NT/CNF, both CNF and ACT–NT were coated and tightly bonded with PPy–NT. This bonding disrupted the hydrogen bonding network between CNF fibers, which typically enhances stiffness and strength. [7,70,71]. In PPy–NT/ACT–NT@1000/CNF_TS1–1, ACT–NT are physically entangled within the PPy–NT/CNF matrix. Moreover, the first synthesis step involves a higher CNF content than PPy–NT (i.e., 60 % CNF vs. 40 % PPy–NT), partially preserving the CNF hydrogen bonding network. This hydrogen bonding network enhances Young's modulus and tensile strength. The arrangement of PPy–NT, CNF and ACT–NT enables CNF to reinforce the composite effectively, improving mechanical strength without compromising the elongation at break. However, increasing the active material loading in PPy–NT/ACT–NT@1000/CNF_TS2–3 led to a sharp decline in Young's modulus (8 MPa) and ultimate tensile strength (0.8 MPa), increasing brittleness. This deterioration is likely due to the disruption of CNF hydrogen bonding interactions caused by higher PPy–NT content (50 % CNF vs. 50 % PPy–NT in the first synthesis step) and the physical entanglement with ACT–NT in the second synthesis step. Notably, all films exhibited an elongation at break below 5 % due to their limited stretchability. Overall, the mechanical properties of the films are primarily governed by the CNF hydrogen bonding network, with ACT–NT playing a minor reinforcing role compared to CNF.

According to Fig. 6, the electrical conductivity of the PPy–NT-based electrode films follows the same trend as that of the incorporated fillers (Fig. 4c-d), highlighting a strong correlation between filler conductivity and the overall electrode performance. PPy–NT/CNF exhibited the highest conductivity (5.9 S cm^{-1}), though still lower than that of pure PPy–NT powder (Fig. 4c-d) due to the insulating nature of CNF. Unlike most reports in the literature [21,72,73], our recently developed one-pot synthesis of PPy–NT/CNF yields superior conductivity in CNF-based conducting polymer composites [52]. This method promotes the formation of supramolecular PPy–NT structures, uniformly deposited onto CNF via a structure-directing agent, enabling the creation of a continuous conductive network [74,75].

Interestingly, adding carbonaceous fillers reduced electrical conductivity. Among these, PPy–NT/CB/CNF retained the highest conductivity (4.1 S cm^{-1}), outperforming ACT–NT-containing electrodes. PPy–NT/ACT–NT@850/CNF and PPy–NT/ACT–NT@1000/CNF displayed conductivities of 0.4 and 1.2 S cm^{-1}, respectively. Despite having the same composition, PPy–NT/ACT–NT@1000/CNF_TS1–1 showed lower conductivity (0.5 S cm^{-1}) than PPy–NT/ACT–NT@1000/CNF. This reduction likely results from ACT–NT@1000 fillers being physically entangled with PPy–NT/CNF, obstructing the conductive pathways of PPy–NT (the most conductive component in the composite). Increasing the PPy–NT loading in PPy–NT/ACT–NT@1000/CNF_TS2–3 slightly enhanced the conductivity (0.7 S cm^{-1}). Conversely, in PPy–NT/ACT–NT@1000/CNF, CNF and ACT–NT@1000 are uniformly coated and closely bonded with PPy–NT, facilitating better electronic transport pathways.

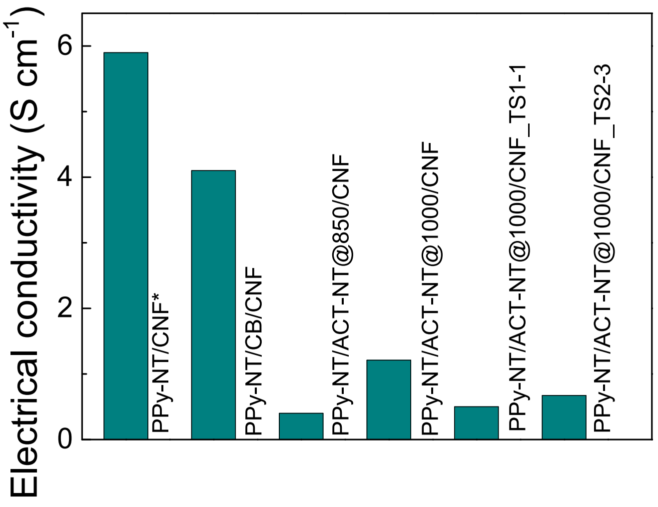

Fig. 6. Electrical conductivity of PPy–NT-based electrode films. *: [52].

3.4. Electrochemical properties of the electrodes and assembled supercapacitors

The electrochemical properties of the PPy–NT-based electrodes were evaluated using both three-electrode and two-electrode configurations, with the latter conducted in a custom-designed T-cell.

Fig. 7a shows the CV curves of the PPy–NT-based electrodes measured in a three-electrode configuration, within a potential window of −0.5 to 0.15 V vs. MSE at a scan rate of 5 mV s^{-1}. All CV curves display a quasi-rectangular shape, typical of pseudocapacitive materials [76,77]. No distinct redox peaks of PPy–NT were observed, likely due to the limited upper potential applied to prevent oxidative degradation of PPy [78–81]. However, subtle distortions related to the redox behavior of PPy [82] can be observed, mainly at the upper edge of the applied potential range. Fig. 7b presents the specific capacitances calculated

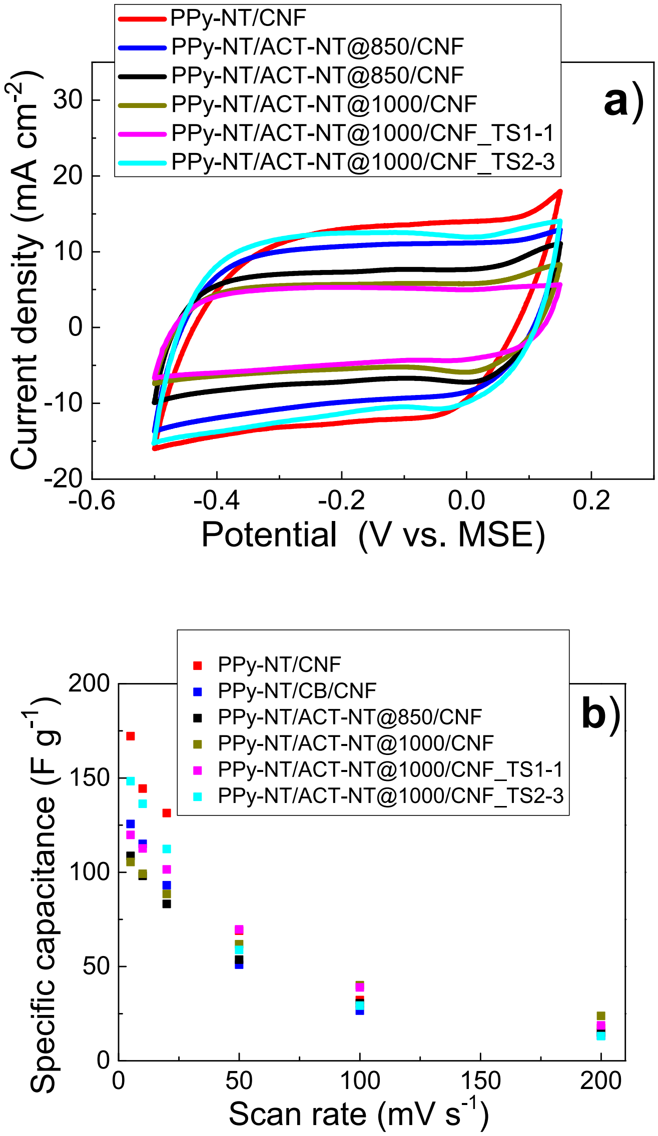

Fig. 7. CV measurements of PPy–NT-based electrodes: a) CV curves recorded at a scan rate of 5 mV s^{-1}, and b) Specific capacitances calculated from CV data at various scan rates.

from the CVs recorded at various scan rates (200, 100, 20, 10, 5 mV s^{-1}), with the corresponding curves shown in Fig. S7. At lower scan rates, the CVs maintained a near-rectangular shape with a steady current, indicating good capacitive behavior. As expected, the specific capacitance decreased with increasing scan rate, due to increased ohmic resistance, charge transfer limitations, and slower ion diffusion at higher scan rates [83]. As shown in Fig. 7b, PPy–NT/CNF exhibited the highest specific capacitance among all tested electrodes (172 F g^{-1} at 5 mV s^{-1}), which can be attributed to its superior electrical conductivity and wettability. These properties improve the utilization of the charge storage capacity of PPy. Under the same conditions, the electrodes containing carbonaceous fillers and prepared via one-pot synthesis exhibited lower specific capacitances: 126 F g^{-1} for PPy–NT/CB/CNF, 109 F g^{-1} for PPy–NT/ACT–NT @850/CNF, and 105 F g^{-1} for PPy–NT/ACT–NT@1000/CNF. This trend closely follows the differences in their electrical conductivities. The PPy–NT/ACT–NT@1000/CNF_TS1–1 electrode, synthesized via a two-step method, achieved a specific capacitance of 120 F g^{-1}, higher than its one-step counterpart. This enhancement is attributed to the improved accessibility and utilization of the hierarchically porous ACT–NT@1000 structure, which features a high S$_{BET}$ and a balanced distribution of micro-and mesopores). Such architecture plays a key role in optimizing the EDL formation during the electrochemical processes [4,84]. In contrast, for the one-pot electrode (PPy–NT/ACT–NT@1000/CNF), the direct polymerization of PPy–NT on the surface of ACT–NT@1000 likely blocked part of its porous structure, reducing the available S$_{BET}$ for charge storage. As expected, increasing the PPy–NT content in PPy–NT/ACT–NT@1000/CNF_TS2–3 improved the specific capacitance to 148 F g^{-1}, approaching that of PPy–NT/CNF. However, despite the higher active material loading, its capacitance remains slightly lower. This is likely due to the reduced electrical conductivity, of this electrode, as the physically entangled ACT–NT@1000 fillers with PPy–NT/CNF in the composite hinder electron transport through the PPy–NT network.

At higher scan rates (from 100 mV s^{-1}), all electrodes exhibited similar specific capacitance values, indicating a reduced contribution from faradaic reactions and a stronger reliance on the EDLC.

GCD measurements were conducted in the same three-electrode configuration to further evaluate the electrochemical performance of the PPy–NT-based electrodes. These tests were performed at various constant current densities (31.1, 15.5, 6.2, 3.1, 1.6, and 0.6 mA cm^{-2}), with the corresponding GCD curves shown in Fig. S8. The specific capacitance values as a function of current density, derived from these GCD measurements, are presented in Fig. 8a. Consistent with the CV results, all the electrodes exhibited a typical decrease in specific capacitance with increasing current density. This trend is due to increased electrode polarization, which limits the effective utilization of PPy–NT during the charge-discharge cycles [4,79,85]. Among all tested electrodes, PPy–NT/CNF exhibited the highest specific capacitance (192 F g^{-1} at 0.6 mA cm^{-2}). This performance is due to the uniform deposition of PPy–NT on the CNF surface, forming a tightly interconnected network that facilitates efficient charge carrier transport and faradaic reactions [86]. Across the entire current density range, electrodes containing carbonaceous fillers followed this trend in specific capacitances: PPy–NT/ACT–NT@1000/CNF_TS2–3 > PPy–NT/CB/CNF > PPy–NT/ACT–NT@1000/CNF_TS1–1 ≈ PPy–NT/ACT-NT@850/CNF ≈ PPy–NT/ACT–NT@1000/CNF. Although PPy–NT/ACT–NT@1000/CNF_TS2–3 had the highest active material content, comparable to PPy–NT/CNF, it still showed lower specific capacitances. This drop is likely due to its lower electrical conductivity, as the physical integration of ACT–NT@1000 may disrupt the conductive network of the PPy–NT matrix. Interestingly, owing to its unique morphology, enhanced electrical conductivity and superior S$_{BET}$ of CB, PPy–NT/CB/CNF demonstrated higher specific capacitances compared to ACT–NT-based electrodes with the same ratio of PPy–NT to carbonaceous fillers and CNF. At lower current densities (e.g., 0.6 mA cm^{-2}), the faradaic redox processes dominate the charge storage mechanism, which explains the observed trend in the specific capacitance values among the electrodes. As current density increases, the specific capacitances of the electrodes containing carbonaceous fillers approach that of PPy–NT/CNF, due to the significant contribution of the EDLC from the carbonaceous fillers. For instance, at the highest current density (31.1 mA cm^{-2}), PPy–NT/ACT–NT@1000/CNF_TS2–3 surpasses all other electrodes, including a slight edge over PPy–NT/CNF, due to the combined contributions of both EDLC and faradaic charge storage. This enhanced performance results from several favourable and well-balanced factors: the amount of active material, the ratio of PPy–NT to ACT–NT and CNF, good electrical conductivity, favourable morphology, and improved accessibility and utilization of the high S$_{BET}$ of ACT–NT@1000, which features well-balanced microporosity and mesoporosity. Despite the promising electrochemical performance of PPy–NT/ACT–NT@1000/CNF_TS2–3, its poor mechanical properties (high brittleness) prevented it from being evaluated in a two-electrode configuration undergoing mid-term stability tests under either the three- or two-electrode configurations.

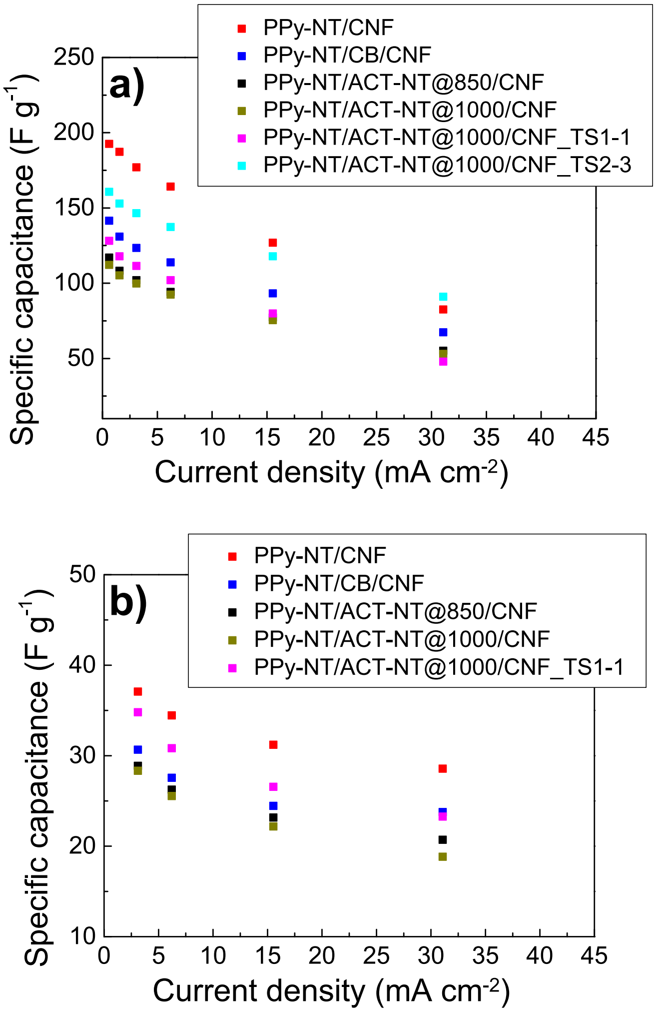

Fig. 8. Specific capacitances of PPy–NT-based electrodes evaluated from GCD measurements: a) in a three-electrode configuration within a potential range of −0.5 to 0.15 V vs. MSE, and b) in a two-electrode configuration within a voltage range of 0 to 0.5 V.

The PPy–NT-based electrodes were subsequently tested in a two-electrode configuration, using a cellulose hydrogel as both a separator and an electrolyte reservoir (1 M H$_2$SO$_4$ solution). Notably, EIS measurements showed that devices incorporating cellulose hydrogel exhibited ohmic resistance values comparable to those using the commercially available Cellgard 5550 microporous separator. A comparison of the area-specific ohmic resistance values for cells with different separators is presented in Fig. S10 (the corresponding Nyquist diagrams for the PPy–NT-based supercapacitors are shown in Fig. S9). These findings suggest that the cellulose hydrogel developed in this study is a competitive alternative to commercial petroleum-based separators.

Similar to the testing conducted in the three-electrode setup, a series of GCD measurements were performed at various current densities (31.1, 15.5, 6.2 and 3.1 mA cm^{-2}) within a voltage range of 0–0.5 V. The GCD curves of the fabricated symmetric devices are displayed in Fig. S11, with the corresponding results shown in Fig. 8b. Key parameters, such as ESR *CE*, *EE* and VE are summarized in Table S6. In general, a slight decrease in *CE* is observed as the current density of the galvanostatic cycling decreases. This suggests the presence of irreversible parasitic reactions, which become more prominent with longer GCD cycles. Nevertheless, in most of the experiments, the *CE* remains above 90 %. In all cases, the ESR values remain stable across different current densities applied to the supercapacitors. As shown in Fig. 8b, in this setup, PPy–NT/CNF achieved the highest specific capacitance across the entire current density range. The specific capacitances follow the trend: PPy–NT/CNF > PPy–NT/ACT–NT@1000/CNF_TS1–1 > PPy–NT/CB/CNF > PPy–NT/ PPy–NT/ACT-NT@850/CNF ≈ PPy–NT/ACT–NT@1000/CNF. Interestingly, PPy–NT/ACT–NT@1000/CNF_TS1–1 exhibited a higher specific capacitance than PPy–NT/CB/CNF, particularly at lower current densities, despite having lower electrical conductivity. At 0.6 mA cm^{-2}, its specific capacitance approaches that of PPy–NT/CNF (e.g., 37 F g^{-1} for PPy–NT/CNF and 35 F g^{-1} for PPy–NT/ACT–NT@1000/CNF_TS1–1). These results highlight the significant role of S_{BET} and the accessibility of the hierarchically porous network in the carbonaceous fillers during the electrochemical processes. They also reflect the dual contribution of both EDLC and faradaic charge storage mechanisms. Although CB has a higher S_{BET} than ACT–NT@1000 and PPy–NT/CB/CNF displays better electrical conductivity than PPy–NT/ACT–NT@1000/CNF_TS1–1, the partial coverage of the porous network of CB during pyrrole polymerization adversely impacts the electrochemical properties in the two-electrode configuration. Similarly, PPy–NT/ACT–NT@1000/CNF displayed lower specific capacitance than PPy–NT/ACT–NT@1000/CNF_TS1–1, despite its higher electrical conductivity. When comparing the one-step synthesis electrodes, PPy–NT/CB/CNF achieved higher specific capacitance across all current densities than the ACT–NT-based electrodes. This is due to higher intrinsic S_{BET} of CB and the enhanced electrical conductivity of the electrode. Overall, the enhanced performance of PPy–NT/ACT–NT@1000/CNF_TS1–1, compared to its one-step synthesis counterparts, can be attributed to the optimal balance of electrical conductivity, morphology, wettability and textural properties (S_{BET} and the effective accessibility of the well-balanced microporosity/mesoporosity of the carbonaceous fillers to the electrolyte). From two-electrode GCD measurements, energy density and power density were evaluated for Ragone plot (Fig. S12). The highest energy density of 1.28 Wh kg^{-1} was achieved by PPy-NT/CNF supercapacitor at a power density of 31.74 W kg^{-1}.

Mid-term cycling stability tests, consisting of 500 GCD cycles in a three-electrode configuration, were performed at a constant current density of 6.2 mA cm^{-2} within a potential range of −0.5 to 0.15 V vs. MSE (Fig. 9a). For selected electrodes, i.e., PPy–NT/CNF and PPy–NT/ACT–NT@1000/CNF_TS1-1, extended stability testing of up 1000 GCD was performed (Fig. S13). All electrodes exhibited a significant initial capacitance loss during the first 100 cycles, followed by a slower decline in the subsequent cycles. Contrary to earlier electrochemical results, the performance of PPy–NT/CNF did not outperform electrodes containing carbonaceous fillers with high S_{BET}, such as CB and ACT–NT@850, despite having the highest initial specific capacitance. Among all electrodes, PPy–NT/ACT–NT@1000/CNF displayed the lowest specific capacitance, likely due to the considerably lower S_{BET} of ACT-NT@1000 compared to ACT–NT@850 and CB. On the other hand, PPy–NT/ACT–NT@1000/CNF_TS1-1 showed better electrochemical performance than the electrodes containing CB and ACT–NT@850, likely due to the improved accessibility of the micropores and mesopores of ACT–NT@1000 by the electrolyte. The capacity retention after 500 cycles (calculated as a difference between the 5th and 500th cycle) ranged from 77 % to 89 % (Table 2). The electrodes with the highest initial specific capacitance, i.e., PPy–NT/CNF and PPy–NT/CB/CNF, showed

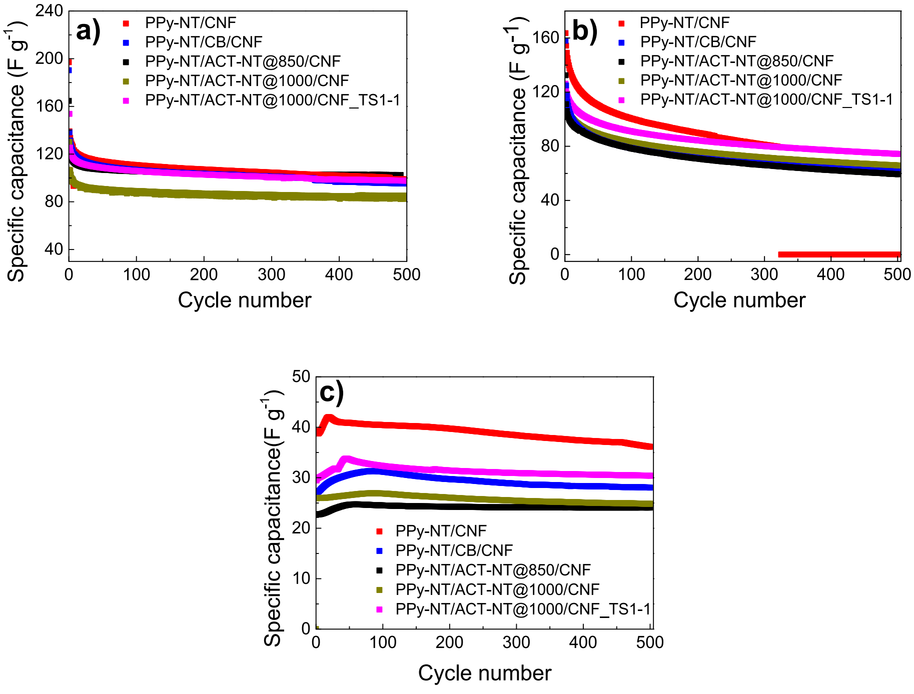

Fig. 9. Specific capacitances of PPy–NT-based electrodes evaluated from GCD mid-term stability measurements: a) three-electrode configuration within a potential range of −0.5 to 0.15 V vs. MSE, b) three-electrode configuration within a potential range of −0.5 to 0.3 V vs. MSE, c) two-electrode configuration within a voltage range of 0 to 0.5 V.

Table 2
Capacity retention of PPy–NT-based electrodes after 500 cycles in various configurations and potential ranges.

Sample name	Capacitance retention in three-electrode configuration (-0.5 to 0.15 V)[a] (%)	Capacitance retention in three-electrode configuration (-0.5 to 0.3 V)[a] (%)	Capacitance retention in two-electrode configuration (0 to 0.5 V)[a] (%)
PPy–NT/CNF	77	0	93
PPy–NT/CB/CNF	77	57	102
PPy–NT/ACT–NT@850/CNF	89	59	106
PPy–NT/ACT–NT@1000/CNF	83	61	96
PPy–NT/ACT–NT@1000/CNF_TS1-1	83	64	101

[a] Capacity retention between the 5th cycle and the 500th cycle.

slightly lower retention, likely due to greater structural or electrochemical deterioration associated with higher charge storage activity. The observed capacitance decay within the potential range of -0.5 to 0.15 V vs. MSE is primarily attributed to the well-documented structural instability of conducting polymers, including PPy–NT, resulting from repeated volumetric shrinking and swelling during the charge/discharge cycles [87]. The addition of carbonaceous fillers with high S_{BET} and good electrolyte accessibility significantly enhances electrochemical performance by contributing to the EDLC. Thus, the promising electrochemical performance of PPy–NT/CB/CNF, PPy–NT/ACT–NT@850/CNF and PPy–NT/ACT–NT@1000/CNF_TS1–1 correlates with the dual contribution of both EDLC and charge storage via faradaic processes.

GCD mid-term stability tests were also conducted at same current density, but within a wider potential range of -0.5 to 0.3 V vs. MSE (Fig. 9b). All electrodes exhibited a significant increase in capacitance decay, particularly during the first 100 cycles. While PPy–NT/CNF displayed the highest specific capacitance up to 300 cycles, its performance dropped sharply to 0 F g^{-1} after 350 GCD cycles. At electrode potentials above 0.15 V vs. MSE, PPy–NT underwent significant volumetric changes due to swelling (during doping, i.e., oxidation) and contraction (during de-doping, i.e., reduction). These changes induce mechanical strain in the polymer, which can compromise the electrochemical performance of the electrode by causing partial detachment of the active material from the bulk of the electrode. In accordance with the literature [4,27,28,82], electrodes containing carbonaceous fillers showed considerably better cycling stability, retaining approximately 60 % of their initial specific capacitance after 500 cycles (see Table 2). This is due to the ability of the fillers to mitigate the volumetric changes of PPy–NT during redox processes.

Before and after mid-term GCD stability cycling within the wider potential range, the electrodes were characterized by CV to analyze the changes in their electrochemical performance due to the cycling. The initial CV (Fig. S14) revealed the redox behavior of PPy–NT, with an oxidation peak at +0.2 V vs. MSE and a reduction peak at -0.1 V vs. MSE. These peaks were more pronounced in the PPy–NT/CNF electrode but were also discernible, though less intense, in the CV curves of electrodes containing carbonaceous fillers. After 500 GCD cycles, the redox peaks in the CV curves were significantly diminished, indicating a reduction in the reversible redox doping/de-doping process of PPy–NT. Raman spectroscopy results (Fig. S5 and Fig. S15) of the electrodes before and after cycling within the wider potential range showed that all electrodes, including PPy–NT/CNF, retained the characteristic peaks of PPy–NT, indicating no significant changes to the chemical structure of PPy–NT after 500 GCD cycles. In addition, SEM images (Fig. 5 and Fig. S16) revealed that all electrodes retained their nanostructured morphology following GCD cycling. Thus, despite a clear capacitance decay and a reduction in the intensity of the PPy–NT redox peaks, the chemical structure and morphology of the electrodes remained largely unchanged within the sensitivity limit of the devices. This suggests that the capacity loss observed in PPy–NT/CNF, which dropped to 0 F g^{-1} after 350 GCD cycles, was likely due to volumetric changes associated with the swelling and shrinking of PPy–NT, which induced mechanical strain and compromised the integrity polymer [23,88]. This loss of mechanical integrity was also visually apparent. The addition of carbonaceous fillers enhanced the mechanical stability to the electrodes during cycling, mitigating some of the structural degradation.

The mid-term cycling stability was similarly tested in a two-electrode configuration, using cellulose hydrogel electrolyte as the electrode separator at a constant current density of 6.2 mA cm^{-2} within a voltage range of 0 to 0.5 V (Fig. 9c). Following the trend observed in two-electrode GCD measurements at different current densities (Fig. 8b), the specific capacitances of the electrodes across the entire range exhibited the following order: PPy–NT/CNF > PPy–NT/ACT–NT@1000/CNF_TS1–1 > PPy–NT/CB/CNF > PPy–NT/ PPy–NT/ACT-NT@850/CNF ≈ PPy–NT/ACT–NT@1000/CNF. This ranking highlights the superior performance of PPy–NT/CNF in the two-electrode configuration, owing to its higher electrical conductivity, improved wettability, and efficient faradaic redox processes, as detailed in Fig. 8b.

Interestingly, unlike in the three-electrode configuration, all electrodes tested in the two-electrode configuration exhibited a slight initial increase in specific capacitance. This behavior can be attributed to improved electrode wetting during the initial cycles, facilitated by interactions with the cellulose hydrogel electrolyte [89–91]. Following this initial rise, a gradual decrease in specific capacitance was observed, beginning after 20 cycles for PPy–NT/CNF, 45 cycles for PPy–NT/ACT–NT@1000/CNF_TS1–1, 60 cycles for PPy–NT/ACT–NT@850/CNF, 70 cycles for PPy–NT/ACT–NT@1000/CNF and 80 cycles for PPy–NT/CB/CNF. PPy–NT/CNF, which exhibited the highest initial specific capacitance and the fastest early-cycle increase, also demonstrated a significantly faster rate of capacitance decay. Its capacity retention after 500 cycles was 96 %, calculated between the 5th and the 500th cycles (see Table 2). This decline is primarily attributed to the structural degradation of PPy–NT, as discussed earlier, and occurred at a notably faster rate compared to electrodes containing carbonaceous fillers.

Among the carbonaceous filler-based electrodes, PPy–NT/ACT–NT@1000/CNF_TS1-1 displayed the most enhanced electrochemical performance, likely due to the optimal balance of electrical conductivity, morphology, wettability and favourable textural properties, as previously detailed. Notably, EIS measurements revealed that the ohmic resistance of the symmetric supercapacitors remained largely unchanged throughout the mid-term stability testing (Table S7). It is also important to note that the specific capacitances recorded in the three-electrode configuration were significantly lower than those observed in the two-electrode configuration. This is expected, as in a symmetrical supercapacitor, the total device capacitance is theoretically equal to half the capacitance of a single electrode, as described by Eq. (10).

$$\frac{1}{C_{sp,cell}} = \frac{1}{C_{sp,el1}} + \frac{1}{C_{sp,el2}} \tag{10}$$

At lower current densities, the difference in specific capacitance measured in the three-electrode configuration becomes especially pronounced, often exceeding 50 %, compared to values obtained in the two-electrode configuration. These generally lower capacitance values in the two-electrode configuration, as well as the partial discrepancies observed in the capacitance trends among different electrode materials, can be attributed to the differing potential ranges applied to the individual electrodes in the respective setups. In the symmetric two-electrode configuration, where identical electrode materials on both sides of the supercapacitor, the potential window of each electrode inherently limited. To prevent overoxidation of PPy–NT and its associated rapid capacitance degradation (see Fig. 9), the overall cell voltage was limited a maximum of 0.5 V. This constraint ensures that the potential of the positive electrode does not exceed 0.15 V vs. MSE. Fig. S17 presents the evolution of individual electrode potentials and the corresponding cell voltage during the initial 20 GCD cycles. Within this voltage range, the available faradaic capacity of PPy–NT, both for oxidation at the positive electrode and reduction at the negative electrode, directly impacts the total initial capacitance of the symmetric full-cell. As such, the observed performance limitations are inherently linked to the electrochemical characteristics of PPy–NT and the narrower voltage potential range enforced in the two-electrode configuration.

Table S9 presents the electrochemical performance of our developed electrodes i.e., PPy-NT/CNF and PPy–NT/ACT–NT@1000/CNF_TS1–1) in comparison with the most relevant cellulose-based electrodes reported in the literature. Direct comparisons of specific capacitance for cellulose-based electrodes are challenging due to variations in experimental conditions (e.g., current density, scan rate) and differing reporting methods for specific capacitance (gravimetric, volumetric, or areal units) across literature sources. Therefore, direct comparisons of these results should be conducted with caution, as they can conceal several potential pitfalls.

Both electrodes (PPy-NT/CNF and PPy–NT/ACT–NT@1000/CNF_TS1–1) presented in this study exhibit promising characteristics and properties across various parameters. The preparation procedure was conducted in an aqueous medium using a conducting polymer as a binder, both of which are environmentally friendly. As shown in Table S9, these electrodes achieved specific capacitance 193 F g-1 at 0.63 mA cm-2 for PPy-NT/CNF and 128 F g-1 at 0.63 mA cm-2 for PPy–NT/ACT–NT@1000/CNF_TS1–1 (calculated based on the total mass of the electrode). The obtained capacity retentions of this work are satisfactory and comparable with previously reported results (Table S9).

4. Conclusion

This study presents a novel and straightforward strategy for the development of a fully renewable supercapacitor, incorporating flexible PPy–NT-based electrodes and a cellulose hydrogel electrolyte/separator. The cellulose hydrogel, offering both flexibility and stability was prepared using a simple, highly reproducible, and sustainable method. The PPy–NT-based electrodes (150 μm thick) were composed of nanostructures of PPy–NT, CNF, and uniquely engineered one-dimensional nitrogen-doped carbonaceous fillers (designed as ACT–NT) or CB, synthesized via environmentally friendly one-pot or two-step methods. The ACT–NT were derived from pre-synthesized PPy–NT via carbonization and subsequent activation. Among them, ACT–NT@1000 exhibited a higher graphitic N content and better electrical conductivity, albeit a lower S_{BET} compared to ACT–NT@850.

All PPy–NT-based electrodes, prepared with a CNF-to-active material ratio of 50:50 *w*/w%, displayed excellent mechanical flexibility despite varying in tensile strength and Young modulus. Morphological analysis confirmed the formation of nanotubular structure of PPy, facilitated by the presence of methyl orange morphology during in situ polymerization. The addition of ACT–NT preserved this nanotubular morphology, and yielded better filler dispersion than CB, tended to form large aggregates. Notably, PPy–NT/CNF exhibited the highest electrical conductivity of 5.9 S cm^{-1}, attributed to its unique morphology and uniform distribution.

Electrochemical characterization in both three- and two-electrode configurations revealed that PPy–NT/CNF delivered the highest specific capacitance during initial GCD cycles. However, over prolonged cycling, electrodes containing ACT–NT or CB exhibited superior capacity retention, particularly within under extended potential window, due to mechanical reinforcement provided by the carbonaceous fillers. These fillers helped mitigate structural degradation arising from the repetitive swelling and shrinking of PPy–NT during redox cycling. Furthermore, their inclusion introduced EDLC contributions, complementing the pseudocapacitive behavior of PPy–NT and enhancing cyclic stability.

Interestingly, the nitrogen doping level and electrical conductivity of the carbonaceous fillers had only a minor impact on overall electrochemical performance. In contrast, the preparation method significantly influenced electrode behavior. Electrodes prepared via the two-step method outperformed their one-pot counterparts. This enhanced performance is attributed to an optimized combination of electrical conductivity, morphology, wettability, textural properties and mechanical robustness.

CRediT authorship contribution statement

Tomáš Lapka: Writing – review & editing, Writing – original draft, Visualization, Validation, Methodology, Investigation, Formal analysis. **Petr Mazúr:** Writing – review & editing, Validation, Supervision, Resources, Methodology. **Jan Prokeš:** Visualization, Investigation. **Miloslav Lhotka:** Investigation. **Marek Jurča:** Investigation. **Marcela Dendisová:** Investigation. **Ondřej Jankovský:** Writing – review & editing, Investigation. **Fatima Hassouna:** Writing – review & editing, Writing – original draft, Validation, Supervision, Resources, Project administration, Methodology, Funding acquisition, Data curation, Conceptualization.

Declaration of competing interest

The authors declare that they have no known competing financial interests or personal relationships that could have appeared to influence the work reported in this paper.

Acknowledgments

The authors would like to thank the Czech Science Foundation (GAČR No. 23-05784S) for the financial support. Additionally, the infrastructure used was made available through project No. CZ.02.01.01/00/22_008/0004617 “Energy conversion and storage (ECO&Stor)”, funded by the European Union and the state budget of the Czech Republic within the framework of the Jan Amos Komensky Operational Program. The authors would like to thank also the Specific University Research (A2_FCHI_2024_021).

Appendix A. Supplementary data

Supplementary data to this article can be found online at https://doi.org/10.1016/j.est.2025.117046.

Data availability

The data supporting this study are publicly available at https://doi.org/10.5281/zenodo.14467876

References

[1] X. Wang, et al., Flexible energy-storage devices: design consideration and recent progress, Adv. Mater. 26 (28) (2014) 4763–4782.
[2] Poonam, et al., Review of supercapacitors: materials and devices, J. Energy Storage 21 (2019) 801–825.
[3] Y. Wang, et al., Flexible supercapacitor: overview and outlooks, J. Energy Storage 42 (2021) 103053.
[4] G. Soukupová, et al., Enhanced specific capacity and cycling stability of flexible nanocellulose-based pseudocapacitive electrodes by controlled nanostructuring of polyaniline, Electrochim. Acta 441 (2023) 141830.

[5] Z. Gui, et al., Natural cellulose fiber as substrate for supercapacitor, ACS Nano 7 (7) (2013) 6037–6046.

[6] Y. Ko, et al., Flexible supercapacitor electrodes based on real metal-like cellulose papers, Nat. Commun. 8 (1) (2017) 536.

[7] R.J. Moon, et al., Cellulose nanomaterials review: structure, properties and nanocomposites, Chem. Soc. Rev. 40 (7) (2011) 3941–3994, https://doi.org/10.1039/c0cs00108b.

[8] G. Siqueira, J. Bras, A. Dufresne, Cellulosic bionanocomposites: a review of preparation, properties and applications, Polymers 2 (4) (2010) 728–765, https://doi.org/10.3390/polym2040728.

[9] W. Zheng, et al., Nanocellulose-mediated hybrid polyaniline electrodes for high performance flexible supercapacitors, J. Mater. Chem. A 5 (25) (2017) 12969–12976.

[10] S. Khodabakhshi, P.F. Fulvio, E. Andreoli, Carbon black reborn: structure and chemistry for renewable energy harnessing, Carbon 162 (2020) 604–649.

[11] C. Chen, et al., Highly strong and flexible composite hydrogel reinforced by aligned wood cellulose skeleton via alkali treatment for muscle-like sensors, Chem. Eng. J. 400 (2020) 125876.

[12] J. Moohan, et al., Cellulose nanofibers and other biopolymers for biomedical applications. A review, Appl. Sci. 10 (1) (2020) 65.

[13] T. Bautkinová, et al., Tailor-made dual doping for morphology control of polyaniline chains in cellulose nanofiber-based flexible electrodes: electrical and electrochemical performance, J. Mater. Sci. 57 (29) (2022) 13945–13961.

[14] C. Chen, et al., Highly conductive nanocomposites based on cellulose nanofiber networks via NaOH treatments, Compos. Sci. Technol. 156 (2018) 103–108.

[15] Y. Yang, C. Chen, D. Li, Electrodes based on cellulose nanofibers/carbon nanotubes networks, polyaniline nanowires and carbon cloth for supercapacitors, Mater. Res. Expr. 6 (3) (2019) 035008.

[16] I. Rabani, et al., The role of uniformly distributed ZnO nanoparticles on cellulose nanofibers in flexible solid state symmetric supercapacitors, J. Mater. Chem. A 9 (19) (2021) 11580–11594.

[17] A.M. Bryan, et al., Conducting polymers for pseudocapacitive energy storage, Chem. Mater. 28 (17) (2016) 5989–5998.

[18] Y. Huang, et al., Nanostructured Polypyrrole as a flexible electrode material of supercapacitor, Nano Energy 22 (2016) 422–438.

[19] I. Shown, et al., Conducting polymer-based flexible supercapacitor, Energy Sci. Eng. 3 (1) (2015) 2–26.

[20] C. Costentin, J.-M. Savéant, Energy storage: pseudocapacitance in prospect, Chem. Sci. 10 (22) (2019) 5656–5666.

[21] M. Lay, et al., Strong and electrically conductive nanopaper from cellulose nanofibers and polypyrrole, Carbohydr. Polym. 152 (2016) 361–369.

[22] A. Aygun, et al., Electrochemically controlled swelling properties of nanoporous templated polypyrrole and layer by layer polypyrrole, J. Electroanal. Chem. 684 (2012) 47–52.

[23] Y. Song, et al., Pushing the cycling stability limit of Polypyrrole for supercapacitors, Adv. Funct. Mater. 25 (29) (2015) 4626–4632.

[24] P. Forouzandeh, V. Kumaravel, S.C. Pillai, Electrode materials for supercapacitors: a review of recent advances, Catalysts 10 (9) (2020) 72.

[25] J. Stejskal, P. Kratochvíl, a. Jenkins, Polyaniline: forms and formation, Collect. Czechoslov. Chem. Commun. 60 (1995).

[26] N.G. Sahoo, et al., Polypyrrole coated carbon nanotubes: synthesis, characterization, and enhanced electrical properties, Synth. Met. 157 (8) (2007) 374–379.

[27] J.-H. Kim, A.K. Sharma, Y.-S. Lee, Synthesis of polypyrrole and carbon nano-fiber composite for the electrode of electrochemical capacitors, Mater. Lett. 60 (13) (2006) 1697–1701.

[28] P. Basnayaka, et al., Graphene/polypyrrole nanocomposite as electrochemical supercapacitor electrode: electrochemical impedance studies, Graphene 02 (2013) 81–87.

[29] S.K. Kandasamy, K. Kandasamy, Recent advances in electrochemical performances of graphene composite (graphene-polyaniline/polypyrrole/activated carbon/carbon nanotube) electrode materials for supercapacitor: a review, J. Inorg. Organomet. Polym. Mater. 28 (3) (2018) 559–584.

[30] J. Wang, et al., Polypyrrole composites with carbon materials for supercapacitors, Chem. Pap. 71 (2) (2017) 293–316.

[31] J. Liu, et al., A novel perspective on interfacial interactions between polypyrrole and carbon materials for improving performance of supercapacitors, Appl. Surf. Sci. 573 (2022) 151626.

[32] Y. Zhu, K. Shi, I. Zhitomirsky, Polypyrrole coated carbon nanotubes for supercapacitor devices with enhanced electrochemical performance, J. Power Sources 268 (2014) 233–239.

[33] T. Lin, et al., Nitrogen-doped mesoporous carbon of extraordinary capacitance for electrochemical energy storage, Science 350 (6267) (2015) 1508–1513.

[34] H. Jin, et al., Heteroatom-doped porous carbon materials with unprecedented high volumetric capacitive performance, Angew. Chem. Int. Ed. Eng. 58 (8) (2019) 2397–2401.

[35] H. Ma, et al., Tailoring the oxygenated groups of graphene hydrogels for high-performance supercapacitors with large areal mass loadings, J. Mater. Chem. A 6 (15) (2018) 6587–6594.

[36] I.-Y. Jeon, H.-J. Noh, J.-B. Baek, Nitrogen-doped carbon nanomaterials: synthesis, characteristics and applications, Chem. Asian J. 15 (15) (2020) 2282–2293.

[37] M. Inagaki, et al., Nitrogen-doped carbon materials, Carbon 132 (2018) 104–140.

[38] Z.R. Ismagilov, et al., Structure and electrical conductivity of nitrogen-doped carbon nanofibers, Carbon 47 (8) (2009) 1922–1929.

[39] Q. Li, et al., A high-performance and flexible electrode film based on bacterial cellulose/polypyrrole/nitrogen-doped graphene for supercapacitors, Carbohydr. Polym. 311 (2023) 120754.

[40] T. Wang, et al., Preparation of foam-like network structure of polypyrrole/graphene composite particles based on cellulose nanofibrils as electrode material, ACS Omega 5 (10) (2020) 4778–4786.

[41] P. Ayala, et al., The doping of carbon nanotubes with nitrogen and their potential applications, Carbon 48 (3) (2010) 575–586.

[42] O.Y. Podyacheva, Z.R. Ismagilov, Nitrogen-doped carbon nanomaterials: to the mechanism of growth, electrical conductivity and application in catalysis, Catal. Today 249 (2015) 12–22.

[43] E.M.M. Ibrahim, et al., Synthesis, characterization, and electrical properties of nitrogen-doped single-walled carbon nanotubes with different nitrogen content, Diam. Relat. Mater. 19 (10) (2010) 1199–1206.

[44] C.Y. Chan, et al., Recent advances of hydrogel electrolytes in flexible energy storage devices, J. Mater. Chem. A 9 (4) (2021) 2043–2069.

[45] Z. Wang, et al., Hydrogel electrolytes for flexible aqueous energy storage devices, Adv. Funct. Mater. 28 (48) (2018) 1804560, https://doi.org/10.1002/adfm.201804560.

[46] T. Xu, et al., Biopolymer-based hydrogel electrolytes for advanced energy storage/conversion devices: properties, applications, and perspectives, Energ. Stor. Mater. 48 (2022) 244–262.

[47] B. Pal, et al., Flexible, ultralight, and high-energy density electrochemical capacitors using sustainable materials, Electrochim. Acta 415 (2022) 140239.

[48] R. Tong, et al., Highly stretchable and compressible cellulose ionic hydrogels for flexible strain sensors, Biomacromolecules 20 (5) (2019) 2096–2104.

[49] Z. Liu, et al., Application of cellulose-based hydrogel electrolytes in flexible batteries, Carbon Neutralization 1 (2) (2022) 126–139.

[50] D. Kasprzak, I. Stępniak, M. Galiński, Electrodes and hydrogel electrolytes based on cellulose: fabrication and characterization as EDLC components, J. Solid State Electrochem. 22 (10) (2018) 3035–3047.

[51] D. Kopecký, et al., Optimization routes for high electrical conductivity of polypyrrole nanotubes prepared in presence of methyl orange, Synth. Met. 230 (2017) 89–96.

[52] T. Lapka, et al., Flexible, ultrathin and light films from one-dimensional nanostructures of polypyrrole and cellulose nanofibers for high performance electromagnetic interference shielding, Carbohydr. Polym. 309 (2023) 120662.

[53] H. Kasparyan, et al., Electromechanical properties of melamine foams covered by polypyrrole nanotubes and carbonaceous fillers, Sensors Actuators A Phys. 351 (2023) 114160.

[54] C. Wu, et al., Cellulose dissolution, modification, and the derived hydrogel: a review, Chemsuschem 16 (21) (2023).

[55] S.H. Zainal, et al., Preparation of cellulose-based hydrogel: a review, J. Mater. Res. Technol. 10 (2021) 935–952.

[56] S.Y. Oh, et al., Crystalline structure analysis of cellulose treated with sodium hydroxide and carbon dioxide by means of X-ray diffraction and FTIR spectroscopy, Carbohydr. Res. 340 (15) (2005) 2376–2391.

[57] G. Soukupová, et al., Novel silicon nanoparticles-based carbonized polypyrrole nanotube composites as anode materials for Li-ion batteries, J. Power Sources 593 (2024) 233976.

[58] J. Stejskal, M. Trchová, Conducting polypyrrole nanotubes: a review, Chem. Pap. 72 (7) (2018) 1563–1595.

[59] X. Yang, et al., Facile fabrication of functional Polypyrrole nanotubes via a reactive self-degraded template, Macromol. Rapid Commun. 26 (21) (2005) 1736–1740.

[60] I. Sapurina, et al., Polypyrrole nanotubes: the tuning of morphology and conductivity, Polymer 113 (2017) 247–258.

[61] J. Stejskal, et al., Comparison of carbonized and activated polypyrrole globules, nanofibers, and nanotubes as conducting nanomaterials and adsorbents of organic dye, Carbon Trends 4 (2021) 100068.

[62] A. Jorio, R. Saito, Raman spectroscopy for carbon nanotube applications, J. Appl. Phys. 129 (2) (2021).

[63] A. Ferrari, J. Robertson, Interpretation of Raman spectra of disordered and amorphous carbon, Phys. Rev. B - Condens. Matter Mater. Phys. 61 (20) (2000) 14095–14107.

[64] J. Stejskal, et al., Conversion of conducting polypyrrole nanostructures to nitrogen-containing carbons and its impact on the adsorption of organic dye, Mater. Adv. 2 (2) (2021) 706–717.

[65] R. Cong, et al., Three-dimensional network of nitrogen-doped carbon matrix-encapsulated Si nanoparticles/carbon nanofibers hybrids for lithium-ion battery anodes with excellent capability, Sci. Rep. 12 (1) (2022) 16002.

[66] B. Xu, et al., Competitive effect of KOH activation on the electrochemical performances of carbon nanotubes for EDLC: balance between porosity and conductivity, Electrochim. Acta 53 (26) (2008) 7730–7735.

[67] G. Ćirić-Marjanović, et al., Synthesis, characterization, and electrochemistry of nanotubular polypyrrole and polypyrrole-derived carbon nanotubes, J. Phys. Chem. C 118 (27) (2014) 14770–14784.

[68] N. Al Habis, et al., Mechanical properties of carbon black/poly (ε-caprolactone)-based tissue scaffolds, Arab. J. Chem. 13 (1) (2020) 3210–3217.

[69] A. Yamakawa, et al., Nanostructure and physical properties of cellulose nanofiber-carbon nanotube composite films, Carbohydr. Polym. 171 (2017) 129–135.

[70] M. Wang, et al., Effect of length of cellulose nanofibers on mechanical reinforcement of polyvinyl alcohol, Polymers 14 (1) (2022) 128.

[71] C.M. Altaner, et al., How cellulose stretches: synergism between covalent and hydrogen bonding, Biomacromolecules 15 (3) (2014) 791–798.

[72] Y. Huo, et al., Multifunctional bacterial cellulose nanofibers/Polypyrrole (PPy) composite films for joule heating and electromagnetic interference shielding, ACS Appl. Electron. Mater. 4 (5) (2022) 2552–2560.
[73] K. Jradi, et al., Characterization of conductive composite films based on TEMPO-oxidized cellulose nanofibers and polypyrrole, J. Mater. Sci. 47 (8) (2012) 3752–3762.
[74] D. Gopakumar, et al., Flexible papers derived from polypyrrole deposited cellulose nanofibers for enhanced electromagnetic interference shielding in gigahertz frequencies, J. Appl. Polym. Sci. 138 (2020).
[75] M. Parit, et al., Polypyrrole and cellulose nanofiber based composite films with improved physical and electrical properties for electromagnetic shielding applications, Carbohydr. Polym. 240 (2020) 116304.
[76] D.A. Bograchev, Y.M. Volfkovich, S. Martemianov, Diagnostics of supercapacitors using cyclic voltammetry: modeling and experimental applications, J. Electroanal. Chem. 935 (2023) 117322.
[77] S. Sharma, P. Chand, Supercapacitor and electrochemical techniques: a brief review, Results Chem. 5 (2023) 100885.
[78] J.B. Schlenoff, H. Xu, Evolution of physical and electrochemical properties of polypyrrole during extended oxidation, J. Electrochem. Soc. 139 (9) (1992) 2397.
[79] T. Lapka, D. Kopecký, P. Mazúr, J. Prokeš, P. Ulbrich, M. Dendisová, M. Sedlačík, F. Hassouna, Elaboration and properties of nanofibrillated cellulose composites with polypyrrole nanotubes or their carbonized analogs, Synth. Met. 278 (2021) 116806.
[80] R. Mazeikiene, A. Malinauskas, Kinetics of the electrochemical degradation of polypyrrole, Polym. Degrad. Stab. 75 (2) (2002) 255–258.
[81] T.F. Otero, M.J. Ariza, Revisiting the electrochemical and polymeric behavior of a polypyrrole free-standing electrode in aqueous solution, J. Phys. Chem. B 107 (50) (2003) 13954–13961.
[82] Y. Zhang, et al., Cellulose nanofibers/reduced graphene oxide/polypyrrole aerogel electrodes for high-capacitance flexible all-solid-state supercapacitors, ACS Sustain. Chem. Eng. 7 (13) (2019) 11175–11185.
[83] M. Kroupa, G.J. Offer, J. Kosek, Modelling of supercapacitors: factors influencing performance, J. Electrochem. Soc. 163 (10) (2016) A2475.
[84] T. Lapka, et al., Elaboration and properties of nanofibrillated cellulose composites with polypyrrole nanotubes or their carbonized analogs, Synth. Met. 278 (2021).
[85] A. Sarkar, G. Gopal Khan, Synthesis of BiFeO3 nanoparticle anchored TiO2-BiFeO3 nano-heterostructure and exploring its different electrochemical aspects as electrode, Mater. Today Proc. 5 (3, Part 3) (2018) 10177–10184.
[86] M.A. Bavio, G.G. Acosta, T. Kessler, Polyaniline and polyaniline-carbon black nanostructures as electrochemical capacitor electrode materials, Int. J. Hydrog. Energy 39 (16) (2014) 8582–8589.
[87] T. Liu, et al., Polyaniline and Polypyrrole Pseudocapacitor electrodes with excellent cycling stability, Nano Lett. 14 (5) (2014) 2522–2527.
[88] P. Bhardwaj, et al., Surfactant decorated polypyrrole-carbon materials composites electrodes for supercapacitor, Diam. Relat. Mater. 108 (2020) 107989.
[89] W.K. Chee, et al., Performance of flexible and binderless polypyrrole/graphene oxide/zinc oxide supercapacitor electrode in a symmetrical two-electrode configuration, Electrochim. Acta 157 (2015) 88–94.
[90] L. Zhang, et al., Skeleton networks of graphene wrapped double-layered polypyrrole/polyaniline nanotubes for supercapacitor applications, J. Mater. Sci. 53 (1) (2018) 787–798.
[91] H. Wang, et al., Graphene-nickel cobaltite nanocomposite asymmetrical supercapacitor with commercial level mass loading, Nano Res. 5 (9) (2012) 605–617.